JGR Solid Earth

RESEARCH ARTICLE
10.1029/2024JB029320

Dynamic Rupture Modeling of Large Earthquake Scenarios at the Hellenic Arc Toward Physics-Based Seismic and Tsunami Hazard Assessment

Sara Aniko Wirp[1,2], **Alice-Agnes Gabriel**[1,3], **Thomas Ulrich**[1], **and Stefano Lorito**[4]

[1]Department of Earth and Environmental Sciences, Ludwig-Maximilians-Universität München, Munich, Germany, [2]GEOMAR Helmholtz Centre for Ocean Research, Kiel, Germany, [3]Scripps Institution of Oceanography, UC San Diego, La Jolla, CA, USA, [4]Istituto Nazionale di Geofisica e Vulcanologia, INGV, Roma, Italy

Key Points:

- We present the first 3D dynamic rupture earthquake scenarios for the Hellenic Arc megathrust
- Epicenter location is a dominant factor controlling the occurrence and intensity of shallow slip and uplift
- Dynamic rupture complexity tends to lower earthquake magnitude but enhances tsunamigenic displacement

Supporting Information:

Supporting Information may be found in the online version of this article.

Correspondence to:

A.-A. Gabriel,
algabriel@ucsd.edu

Citation:

Wirp, S. A., Gabriel, A.-A., Ulrich, T., & Lorito, S. (2024). Dynamic rupture modeling of large earthquake scenarios at the Hellenic Arc toward physics-based seismic and tsunami hazard assessment. *Journal of Geophysical Research: Solid Earth*, *129*, e2024JB029320. https://doi.org/10.1029/2024JB029320

Received 14 APR 2024
Accepted 12 OCT 2024

Author Contributions:

Conceptualization: Sara Aniko Wirp, Alice-Agnes Gabriel
Data curation: Sara Aniko Wirp, Alice-Agnes Gabriel, Thomas Ulrich, Stefano Lorito
Formal analysis: Sara Aniko Wirp, Alice-Agnes Gabriel
Funding acquisition: Sara Aniko Wirp, Alice-Agnes Gabriel
Investigation: Sara Aniko Wirp, Alice-Agnes Gabriel
Methodology: Sara Aniko Wirp, Alice-Agnes Gabriel, Thomas Ulrich
Project administration: Sara Aniko Wirp, Alice-Agnes Gabriel
Resources: Sara Aniko Wirp, Alice-Agnes Gabriel
Software: Sara Aniko Wirp, Alice-Agnes Gabriel, Thomas Ulrich

Abstract

The Mediterranean Hellenic Arc subduction zone (HASZ) has generated several $M_W \geq 8$ earthquakes and tsunamis. Seismic-probabilistic tsunami hazard assessment typically utilizes uniform or stochastic earthquake models, which may not represent dynamic rupture and tsunami generation complexity. We present an ensemble of ten 3D dynamic rupture earthquake scenarios for the HASZ, utilizing a realistic slab geometry. Our simplest models use uniform along-arc pre-stresses or a single circular initial stress asperity. We then introduce progressively more complex models varying initial shear stress along-arc, multiple asperities based on scale-dependent critical slip weakening distance, and a most complex model blending all aforementioned heterogeneities. Thereby, regional initial conditions are constrained without relying on detailed geodetic locking models. Varying epicentral locations in the simplest, homogeneous model leads to different rupture speeds and moment magnitudes. We observe dynamic fault slip penetrating the shallow slip-strengthening region and affecting seafloor uplift. Off-fault plastic deformation can double vertical seafloor uplift. A single-asperity model generates a $M_W \sim 8$ scenario resembling the 1303 Crete earthquake. Using along-strike varying initial stresses results in $M_W \sim 8.0$–8.5 dynamic rupture scenarios with diverse slip rates and uplift patterns. The model with the most heterogeneous initial conditions yields a $M_W \sim 7.5$ scenario. Dynamic rupture complexity in prestress and fracture energy tends to lower earthquake magnitude but enhances tsunamigenic displacements. Our results offer insights into the dynamics of potential large Hellenic Arc megathrust earthquakes and may inform future physics-based joint seismic and tsunami hazard assessments.

Plain Language Summary

The Mediterranean region around Greece and Crete is a hotspot for earthquakes and tsunamis. Here, the tectonic plates of Africa and Europe collide. History shows that this region has experienced damaging earthquakes. These earthquakes can cause tsunamis, sea waves that may lead to widespread destruction along coastlines. Our study aims to understand better how future earthquakes can be modeled. We use computer models to simulate different earthquake scenarios. Initially, we use simple conditions in our models, showing that if an earthquake propagated across the entire region, it could reach a moment magnitude of 9. When we move the earthquake's location within our model, the size and impact of the resulting earthquake change; some locations lead to larger seafloor displacements, which may cause more dangerous tsunamis. When introducing more complicated loading and fault strength conditions, the resulting earthquakes become smaller, consistent with historical observations. We also simulate how the fault-surrounding rocks can deform during an earthquake. Such deformations can increase the uplift of the seafloor, increasing the potential for tsunamis. Our work shows that computer modeling can be a powerful tool for understanding earthquakes and tsunamis and better prepare for future events.

1. Introduction

The Hellenic Arc is the most seismically active structure of the Mediterranean Sea (Ganas & Parsons, 2009; Vannucci et al., 2004). It is formed by the subduction of the African plate beneath the Aegean microplate and extends from Lefkada (western Peloponnese) in the west to east of Rhodes Island (Papazachos et al., 2000; Papazachos & Nolet, 1997; Piromallo & Morelli, 2003).

The northward movement of the African plate at 5 mm/yr (Ganas & Parsons, 2009; Vernant et al., 2014) and the fast southwest movement of the Aegean plate at 30.5 mm/yr (Reilinger et al., 2006) lead to relatively high convergence rates. Across the Hellenic Arc, GNSS inferred velocities are the fastest detected in the entire

Supervision: Sara Aniko Wirp, Alice-Agnes Gabriel
Validation: Sara Aniko Wirp, Alice-Agnes Gabriel
Visualization: Sara Aniko Wirp, Alice-Agnes Gabriel
Writing – original draft: Sara Aniko Wirp, Alice-Agnes Gabriel
Writing – review & editing: Sara Aniko Wirp, Alice-Agnes Gabriel, Thomas Ulrich, Stefano Lorito

Mediterranean Sea (Kahle et al., 2000; McClusky et al., 2000). However, convergence is slower than in seismically very active subduction zones such as in Chile, Alaska, and Java (Bourgois et al., 1996; DeMets et al., 1990, 1994; Elliott & Freymueller, 2020; McCaffrey, 1997; Tregoning et al., 1994) challenging observations of complete seismic cycles.

The slab rollback of the Hellenic Arc subduction forms the megathrust into an oval shape (Bohnhoff et al., 2005; Jolivet et al., 2013). Based on stress inversion using observed earthquake faulting mechanisms, Kkallas et al. (2021) identify five seismotectonic domains (Figure 1). First, the outer Hellenic Arc, characterized by low-angle NW-SE thrust-faulting interface events with typical focal depths between 30 and 40 km, is formed by NE-SW compression. Second, the sedimentary arc, including the islands (e.g., Peloponnese, Crete, and Karpathos), which is dominated by north-south oriented normal faults and earthquakes shallower than 30 km depth. Third, the Volcanic arc formed due to extension in the N-S direction, including normal faults that follow the observed volcanic arc strike. Furthermore, the southeastern Aegean region exhibits a combination of subduction-related faulting and southwest-northeast trending arc-parallel strike-slip faulting (Nyst & Thatcher, 2004), forming the Strabo and Pliny trenches and hosting seismicity with focal depths reaching up to 60 km. In the eastern section of the Hellenic Arc, there is a transition from subduction to different tectonic styles, characterized by a progressive rake rotation from a reverse to a strike-slip dominant mechanism as the convergence becomes more oblique. Finally, deeper (50–160 km) in-slab events are observed along strike-slip faults off the subducted slab and often include a notable thrust component.

When portions of a megathrust are considered to be significantly "coupled", they can accumulate pronounced long-term slip deficits, which may be released in earthquakes. Which portions of the Hellenic Arc are seismically coupled is debated. While Ganas and Parsons (2009) argue that the Hellenic Arc is frictionally fully locked, other authors infer that because of the high convergence rate and relatively low seismicity, a large part of the regional plate convergence must be accommodated aseismically (Becker & Meier, 2010; Jackson & Mckenzie, 1988; Shaw & Jackson, 2010; Vernant et al., 2014), or determine along-strike variations in coupling (Laigle et al., 2004). Becker and Meier (2010) assume periods of seismic locking followed by intermediate moment magnitude events and aseismic slip. Vernant et al. (2014) develop a block model of the Aegean to explore the degree of seismic coupling of the megathrust interface and restrict the seismogenic and fully coupled portion of the Hellenic Arc to 15–45 km depth. They conclude that the absence of crustal shortening and the slip deficit rate of the Hellenic Arc are related to poorly consolidated and saturated sediments and characterize the upper 15 km as aseismic. Shaw and Jackson (2010) state that the plate interface never reaches the surface, and the plate motion discharges in sediment thickening and folding, forming an 8–10 km accretionary prism of thick seafloor sediments that are seismically decoupled from the oceanic crust.

Off-shore areas such as the Hellenic Arc subduction zone are difficult to study due to limited accessibility, specifically for satellite-based geodetic techniques. Additionally, a lack of quantitative data spanning complete seismic cycles of the Hellenic Arc significantly increases the uncertainty regarding the occurrence rate of large earthquakes. Even for recent events that are relatively well-recorded, the detailed rupture process often remains challenging to unravel (e.g., Chousianitis & Konca, 2021; Kiratzi et al., 2022; Ren et al., 2022). The conditions that may enhance or impede future large subduction zone earthquakes in the Hellenic Arc are poorly understood. Important aspects may be, among others, present-day near-trench and depth-extension of the seismic locking, frictional properties, regional stress state, and sediment strength (Du et al., 2021; Jeandet Ribes et al., 2023; Lay et al., 2012; Sallarès & Ranero, 2019; Ulrich et al., 2022; Wilson & Ma, 2021). Specifically, the potential near-surface rupture processes that may control large, vertical seafloor displacements and tsunami hazards are challenging to assess.

Geodetic coupling can help to inform the initial stress conditions of dynamic rupture models (Gu et al., 2023; Hok et al., 2011; Noda et al., 2021; Ramos & Huang, 2019; Yang et al., 2019). The product of slip rate deficit (inferred from seismic coupling studies) and assessed strain accumulation times allows inferring slip deficit distribution and associated static stress change (Ramos & Huang, 2019). Lindsey et al. (2021) show that frictionally unlocked regions above the locked portion of the megathrust can yet exhibit a slip rate deficit of over 80% of the plate convergence rate, which is stress-shadowed by the deeper locked megathrust. However, detailed geodetic constraints are yet unavailable for the Hellenic Arc region.

Dynamic earthquake rupture simulations (e.g., Harris et al., 2018) combine the frictional failure of rocks and seismic wave propagation in a non-linear and multi-physics manner to produce physics-based forecasts and

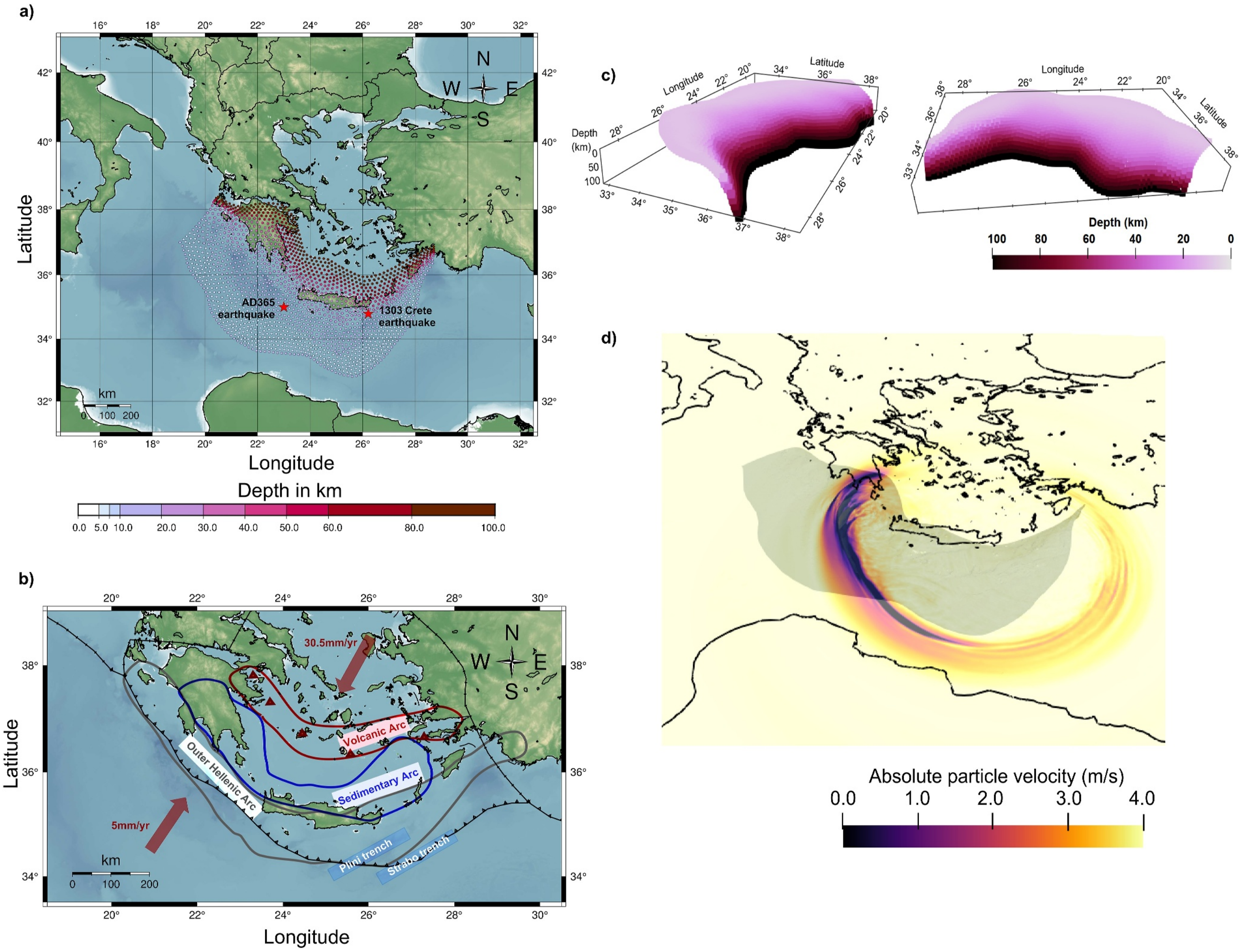

Figure 1. Tectonic constraints for 3D dynamic rupture scenarios in the Hellenic Arc area: (a) Hellenic Arc megathrust geometry (Basili et al., 2013) and modeled domain extent. Depth is colored from shallow (white) to deep (purple). The red stars mark the hypocenters of the historical $M_W \sim 8$ AD 365 and 1303 Crete earthquakes that generated destructive tsunamis. (b) Zoomed-in view of (a) focusing on the northern trench as the main tectonic feature including plate boundaries and motions of the African and Eurasian Plates, and subduction zone domains. The main plate boundaries (Bird, 2003) are marked with black lines. Subduction zones are also labeled with black triangles, pointing toward subduction. Red arrows indicate the Aegean (30.5 mm/yr (Reilinger et al., 2006)) and the African (5 mm/yr (Ganas & Parsons, 2009; Vernant et al., 2014)) plate motions resulting in a convergence rate of ∼35 mm/yr. A gray line frames the outer Hellenic Arc, a blue line frames the Sedimentary Arc, and the Volcanic Arc is framed by a red line (Kkallas et al., 2021). In-slab events lay below the transition from Sedimentary to Volcanic Arc. (c) 3D views of the modeled Hellenic arc megathrust. (d) Modeled absolute particle velocity [m/s] across the Earth's surface with topo-bathymetry in the reference scenario at simulation time 100 s. High-amplitude surface waves extend from Greece and Turkey until the coast of Lybia and Egypt, suggesting that the ground shaking from a margin-wide megathrust event on the Hellenic Arc could directly affect large parts of the eastern Mediterranean.

provide insight into the poorly understood fundamental processes of earthquake faulting. As input, dynamic rupture simulations require, among other parameters, fault geometry, on-fault prestresses, and frictional fault strength descriptions Ramos et al. (2022). This input is generally challenging to constrain observationally, especially in off-shore subduction regions, like the Aegean Sea, with sparse near-trench observations (Ulrich et al., 2022).

We present an ensemble of 10 3D dynamic rupture scenarios of megathrust earthquakes across the Hellenic Arc, including realistic slab geometry, topography, and off-fault plastic deformation, to help address the lack of quantitative observations of historical large earthquakes and a heterogeneous plate coupling model. Our models help better understand how large ruptures may start, propagate, and arrest and which seafloor deformation might result. We develop four large counterfactual scenarios (Woo, 2018) and models that resemble historic tsunamigenic events. Our findings may offer constraints for dynamically plausible slip distributions, tsunami generation mechanisms, and surface deformation, informing future physics-based probabilistic seismic hazard analysis (PSHA), seismic-probabilistic tsunami hazard assessment (S-PTHA), and joint evaluation of seismic and tsunami hazards in subduction zones.

We explore various approaches for realizing 3D dynamic rupture scenarios on the shallowly dipping Hellenic Arc subduction interface. Assuming homogeneous along-arc stresses and varying hypocenter locations result in counterfactual margin-wide rupture scenarios (models HE, HM, and HW). Dynamic rupture scenarios can penetrate velocity-strengthening fault regions and drastically vary in their amount of shallow slip, depending on the hypocenter location. We also assess the effects of off-fault deformation (model HEP) on seafloor displacement. We then analyze an asperity model (HEA) that may resemble the 1303 Crete earthquake, constrained by subduction earthquake scaling relations (Strasser et al., 2010). Next, we explore heterogeneous initial stress conditions constrained by stress inversions (Kkallas et al., 2021) (models HES and HMS) with epicenters located in the east and center of the Hellenic Arc megathrust. When we incorporate prestress variations, the dynamic rupture extent is limited. We explore how increasing initial stress complexity affects rupture propagation, shallow slip, and seafloor displacement. We then implement fractally distributed frictional asperities (model DCA), with size-dependent critical slip-weakening distance (D_c), following Ide and Aochi (2005) and Gallovič and Valentová (2023). Finally, we investigate a model incorporating segmented fault loading and multi-scale asperities (model DCAS). We compare results to existing uplift data in the Hellenic region and discuss implications on tsunami hazards for all dynamic rupture models.

1.1. Historic Tsunamigenic Earthquakes: The AD 365 and 1303 Events

Historically, the Aegean region hosted at least two $M_W \geq 8$ events, both of which generated regional tsunamis: the AD 365 Crete event, located offshore west of Crete, and the 1303 Crete event, located offshore further east between Crete and Karpathos.

The AD 365 earthquake likely occurred due to thrust faulting beneath Crete (Shaw et al., 2008). The exact location and whether or not it was located on the Hellenic Arc subduction interface itself or on a branching splay fault remains unclear (Papazachos & Nolet, 1997; Bohnhoff et al., 2001; Stiros & Drakos, 2006; Shaw et al., 2008; N. Ambraseys, 2009). Due to the earthquake and the associated tsunami, thousands of people were killed (Kelly, 2004; S. C. Stiros, 2020). Archeological observations confirm seismic destruction in Crete (DiVita, 1979, 1995; Markoulaki, 1987). This earthquake may have produced up to ∼9 m coseismic uplift (Flemming, 1978; Pirazzoli et al., 1982, 1992; Stiros & Drakos, 2006; Shaw et al., 2008). Sedimentology, radiocarbon data, field observations, and seamarks around the shore of Crete evidence a tsunami (Scheffers & Scheffers, 2007; Shaw et al., 2008; Spratt, 1865).

Several studies attempted to reproduce the tsunami generated by the historical AD 365 Crete event using different static or kinematic earthquake models (S. Tinti et al., 2005; Papadimitriou & Karakostas, 2008; Shaw et al., 2008; England et al., 2015) with fault lengths ranging from 100 km to more than 200 km, dipping at 20–45°. The earthquake may have occurred on a splay fault branching the main megathrust (Shaw et al., 2008; Shaw & Jackson, 2010; S. C. Stiros, 2010; Saltogianni et al., 2020) or on an antithetic normal fault (Ott et al., 2021), which can explain the high amount of uplift observed on Crete. Papadimitriou and Karakostas (2008) model the AD 365 earthquake on a thrust fault parallel to the megathrust. With a maximum slip of 25 m, a moment magnitude of $M_W 8.4$, and a seafloor uplift of up to ∼9 m near southwest Crete, they can fit observations of co-seismically uplifted coastal material from Pirazzoli et al. (1996). England et al. (2015) use the rupture models of Shaw et al. (2008) and Papadimitriou and Karakostas (2008) as sources for a tsunami simulation. While the source of Shaw et al. (2008) produces a smaller tsunami with wave heights of up to ∼7 m, the model from Papadimitriou and Karakostas (2008) generates wave heights of ∼10 m, which fit observations better.

The 1303 Eastern Crete event is among the best-documented historical events in the Mediterranean Area (Yolsal et al., 2007). It probably occurred on a thrust fault (Yolsal-Çevikbilen & Taymaz, 2012), which might be the Hellenic Arc itself or a smaller fault parallel to the megathrust. The earthquake caused a tsunami that affected a large area and was recorded in Crete, Peloponnese, Rhodes, Cyprus, Antalya in south-west Turkey, Acre in Israel, the Adriatic Sea, and the Alexandria-Nile delta in Egypt (N. N. Ambraseys, 1962; N. N. Ambraseys, 1994; N. Ambraseys, 2009; Antonopoulos, 1980; Guidoboni & Comastri, 1997; Guidoboni et al., 2005; Altinok & Ersoy, 2000; Soloviev et al., 2000; Yolsal et al., 2007).

1.2. Seismic-Tsunami Hazard Assessment in the Hellenic Arc Region

Both historic, devastating, tsunamigenic $M_W \geq 8$ events and more recent, smaller earthquakes in the Hellenic Arc region have motivated local and regional earthquake-tsunami hazard studies (S. Tinti et al., 2005; Lorito et al., 2008; Papoulia et al., 2010; Lorito et al., 2015; Tonini et al., 2011; Grezio et al., 2012; Sørensen et al., 2012; Selva et al., 2016; Davies et al., 2018; Volpe et al., 2019; Scala et al., 2020; Basili et al., 2021; Selva et al., 2021). S. Tinti et al. (2005) simulated tsunamis initiated by sources related to the AD 365 and 1303 Crete earthquakes, which they assumed to be running parallel to the Hellenic megathrust. Lorito et al. (2008) determined the geometry, kinematics, and size of generally feasible maximum moment magnitude events in the Hellenic Arc region and simulated the related tsunamis. They find that these events produce tsunami waves of up to 5 m in height. Sørensen et al. (2012) developed the first S-PTHA model in the Mediterranean area. They find that the tsunami hazard in the eastern Mediterranean is governed by earthquakes along the Hellenic arc and estimate a near 100% probability of tsunami waves exceeding 1 m in the next 30 years. Recent studies (Basili et al., 2021; Scala et al., 2020; Selva et al., 2016) focus on a formal aleatory and epistemic uncertainty quantification in S-PTHA, while including more detailed information on the fault structure and account for the effects on the hazard model of potential shallow slip amplification.

3D dynamic rupture models, simulating spontaneously evolving rupture propagation along the megathrust geometry, have not been explored for the Hellenic arc. Yet, physically consistent earthquake scenarios from 3D dynamic rupture modeling and associated time-dependent surface displacements could complement stochastic earthquake source models typically used in S-PTHA. Stochastic earthquake slip models in combination with efficient tsunami solvers are convenient for S-PTHA (e.g., Davies et al., 2018; McCloskey et al., 2008; Scala et al., 2020), as they are computationally cheap, and therefore allow exploring the expected natural - assumed aleatory - variability of earthquake slip distributions to a great extent. Alternatively, plausible source models may be obtained from kinematic source models of past earthquakes based on seismic inversion data (Lorito et al., 2008; Scala et al., 2020; Song & Somerville, 2010). However, questions regarding their use to constrain potential future events remain; specifically, it remains debated whether information based on past earthquakes is sufficient to constrain the source characteristics of future events. Kinematic source models can be designed to match empirical earthquake scaling laws and to produce a range of magnitudes to aid hazard assessment (e.g., Marafi et al., 2019), but are not necessarily compatible with the physical laws of earthquake faulting (e.g., E. Tinti et al., 2021). Static source models, however, neglect the tsunami-earthquake interaction during the co-seismic seafloor uplift and tsunami generation process. A tsunami can evolve and propagate during its generation phase, especially for long-duration, large, and/or slow earthquakes. This effect is only captured when sourcing the tsunami model using the complete time-dependent co-seismic uplift phase (Abrahams et al., 2023; Madden et al., 2020; Wirp et al., 2021).

3D physics-based earthquake modeling may contribute to a better understanding of earthquake and tsunami source effects, benefiting S-PTHA studies. In particular, it can help to decipher the effects of off-fault damage and heterogeneous on-fault material properties on near-surface slip amplifications and associated seafloor uplift toward a complete understanding of tsunami generation and hazard assessment (Behrens et al., 2021). Dynamic rupture simulations model how earthquakes nucleate, propagate, and arrest in a mechanically self-consistent manner. Due to computational advances, 3D dynamic rupture simulations on the scale of subduction zones are now feasible (Galvez et al., 2016; Hok et al., 2011; Krenz et al., 2021; Ramos & Huang, 2019; Uphoff et al., 2017).

Recent studies (Galvez et al., 2016; Murphy et al., 2016, 2018; Uphoff et al., 2017; Ma & Nie, 2019; Ramos & Huang, 2019; Saito et al., 2019; van Zelst et al., 2022; B. Li et al., 2023) show that physics-based dynamic rupture models of complex fault systems and megathrusts offer feasible source descriptions for tsunami modeling. These models can provide a time-dependent tsunami source by linking the seafloor displacements and velocities to the tsunami model (Amlani et al., 2022; Kutschera et al., 2024; Lotto, Dunham, et al., 2017; Madden et al., 2020; Ryan et al., 2015; Ulrich et al., 2022; Ulrich, Vater, et al., 2019). In this way, the effects of reflected waves at the free-surface in the accretionary wedge (Lotto, Nava, & Dunham, 2017; Nielsen, 1998; van Zelst et al., 2019), spontaneously evolving shallow slip amplification (Ma & Beroza, 2008; Rubin & Ampuero, 2007; Scala et al., 2017) caused by bi-material effects or updip rupture propagation, and the impact of off-fault plastic yielding on seismic ground motions (Roten et al., 2014, 2017; Xu et al., 2015) and seafloor displacements (Ma & Hirakawa, 2013; Ma & Nie, 2019; Ulrich et al., 2022; Wilson & Ma, 2021) can be taken into account.

2. Reference 3D Dynamic Rupture Model Setup

We here describe the reference dynamic rupture modeling parameters and model setup forming the base of all 10 scenarios. We use the open-source software package SeisSol (https://seissol.org) (e.g., de la Puente et al., 2009; Pelties et al., 2012, 2014) on high-performance computing infrastructure. Our SeisSol simulations simultaneously solve for seismic wave propagation, frictional failure on prescribed fault interfaces, and (visco-) plastic Drucker-Prager off-fault plastic deformation (Andrews, 2005; Wollherr et al., 2018). SeisSol is based on an Arbitrary high-order accurate DERivative Discontinuous Galerkin method (ADER-DG) (Dumbser & Käser, 2006; Käser & Dumbser, 2006)). It uses unstructured tetrahedral meshes enabling models incorporating geometrical complexities (e.g., Ulrich, Gabriel, et al., 2019; Wolf et al., 2020; B. Li et al., 2023; Taufiqurrahman et al., 2023), such as the shallowly dipping megathrust interface geometry of the Hellenic Arc. In all models, frictional failure and fault slip are governed by a linear slip weakening friction law (Ida, 1972). We adopt the isotropic version of the 1D velocity model PREM (Preliminary Reference Earth Model) (Bormann, 2009; Dziewonski & Anderson, 1981).

2.1. Geometric Model, Mesh, and Resolution

We build a geometric model of the eastern Mediterranean region, including the Hellenic subduction zone, the Greece and Turkey coastlines, and parts of northern Africa, as well as Italy (Figure 1), incorporating topography and bathymetry (GEBCO Compilation Group, 2019) at 15 arc s or ∼380 m resolution. We use the Hellenic Arc subduction interface geometry from the European Database of Seismogenic Faults (EDSF, Basili et al. (2013)) at ∼0.2° resolution, which is inferred from seismicity distributions, receiver functions, seismic imaging, velocity-gravity models, GPS velocities, geological observations, and topographic analyses. The same fault model was used in recent tsunami hazard studies (Scala et al., 2020; Selva et al., 2016). The modeled slab is 800 km wide, 600 km long, and reaches 90 km depth. Our model domain spans ∼4,400 by ∼2,800 by ∼500 km.

We use an adaptive unstructured tetrahedral mesh, refined toward the fault and the free surface. Our resulting mesh consists of 38.89 million elements. The smallest elements are used to discretize the megathrust fault interface and have a 650 m edge length. We use high-order accuracy in space and time using polynomial basis functions of order $p = 5$. Thus, each triangular element face, which is assigned a dynamic rupture internal boundary condition, is discretized by $(p+2)^2$ Gauss points. This allows adequately resolving the minimum process zone width at the rupture tip, which we measure as ~1,500 m following Wollherr et al. (2018). We calculate the resolution of the seismic wavefield characterized by the maximum frequency resolved according to

$$f \approx V_s/\Delta x/elements\ per\ wavelength \tag{1}$$

with Δx defining the local element size, V_s the s-wave speed, and the minimum required $elements\ per\ wavelength = 2$ for order 6 accuracy in space and time (Käser et al., 2008; Pelties et al., 2014). This mesh resolution allows us to resolve the seismic wavefield up to 2.7 Hz close to the slab. Resolution gradually decreases with static coarsening of the mesh away from the slab interface. However, owing to the relative proximity of the slab to the free-surface, we still achieve a resolution of 1.75 Hz at the free surface above the slab (Figure A1).

2.2. Ambient Prestress and Relative Fault Strength

In all our models, we constrain the tectonic background prestress state and megathrust strength at the subduction scale using a regional stress tensor approach (Ulrich et al., 2022) and seismo-tectonic observations, the Mohr-Coulomb theory of frictional failure, and assumptions on depth-dependent pore fluid pressure. We fully constrain a Cartesian prestress tensor representing a regional ambient loading by constraining the orientation of the maximum compressive principal stress σ_1 (3 angles), the stress shape ratio Φ (Equation 2), the maximum relative prestress ratio $\mathcal{R}_0$ (Equation 3), and the effective vertical stress gradient.

We follow Angelier (1990) and Lund and Townend (2007) to define the stress shape ratio, balancing the principal stress magnitudes, σ_i, as

$$\Phi = \frac{\sigma_2 - \sigma_3}{\sigma_1 - \sigma_3}, \tag{2}$$

Constraining Φ from stress inversions (Kkallas et al., 2021) is challenging. In the following, we assume $\Phi = 0.4$, which is consistent with stress inversion results of interplate events around Crete (Bohnhoff et al., 2005).

Closeness to the onset of frictional failure can be quantified by the relative prestress ratio $\mathcal{R}$ (e.g., Aochi & Madariaga, 2003) defined as:

$$\mathcal{R} = \frac{\Delta\tau}{\Delta\tau_b} = \frac{\tau - \mu_\mathrm{d}\sigma_n'}{c + \left(\mu_\mathrm{s} - \mu_\mathrm{d}\right)\sigma_n}. \tag{3}$$

$\mathcal{R}$ relates the potential stress-drop $\Delta\tau$ to the frictional breakdown strength-drop $\Delta\tau_b$. c is the frictional cohesion, and μ_d and μ_s are the dynamic and static friction coefficients, respectively. The strength parameter S is directly related to $\mathcal{R}$, as $S = \frac{1}{\mathcal{R}} - 1$. We define $\mathcal{R}_0 \geq \mathcal{R}$ as the maximum possible value of $\mathcal{R}$. $\mathcal{R} = \mathcal{R}_0$ for faults optimally orientated toward the regional stress tensor. $\mathcal{R}_0 = \mathcal{R} = 1$ would characterize a critically prestressed optimally oriented fault. For all models, we define their relative fault strength with respect to the frictional strength drop. We use $\mathcal{R}_0 = 0.7$ ($S = 0.43$), implying that fault stress drop can reach a maximum of 70% of the breakdown strength drop. This is large enough to propagate earthquake rupture on a significant portion of the megathrust but small enough to ensure realistic rupture characteristics such as rupture speed and stress drop.

Many megathrusts are characterized by non-Andersonian prestress conditions, particularly in regions with complex tectonics (Hardebeck, 2015). The crust in the Mediterranean Sea is comparably old and cold (Bocchini et al., 2020; Granot, 2016; Müller et al., 2008; Speranza et al., 2012) potentially implying a low-stress environment. We constrain the stress shape ratio from stress inversion results of Bohnhoff et al. (2005). In all our models, we assume a non-Andersonian prestress state, where none of the principal stresses is purely vertically oriented (Figure 2). In the reference prestress model, used in scenarios HE, HM, HW, HEP, and DCA (as defined in Figure 2 and Sections 1 and 3), the maximum compressive stress, σ_1, is assumed shallowly plunging, σ_2 is horizontal, and σ_3, normal to the $\sigma_1 - \sigma_2$ plane, is steeply plunging. Through static analysis and trial-and-error dynamic rupture simulation, we selected this pre-stress condition to optimally pre-stress the slab in the hypocentral region of the reference prestress model setup.

The components of the stress tensor are defined as follows:

$$\sigma_{zz}'(z) = \rho g z - P_f(z) \tag{4}$$

$$\sigma_{xx}'(x,y,z) = \Omega\Big(b_{xx}\Big(\sigma_{zz}'(z) + P_f(z)\Big) - P_f(z)\Big) + (1+\Omega)\sigma_{zz}'(z), \tag{5}$$

$$\sigma_{yy}'(x,y,z) = \Omega\Big(b_{yy}\Big(\sigma_{zz}' + P_f(z)\Big) - P_f(z)\Big) + (1+\Omega)\sigma_{zz}'(z), \tag{6}$$

$$\sigma_{xy}'(x,y,z) = \Omega\Big(b_{xy}\Big(\sigma_{zz}'(z) + P_f(z)\Big) - P_f(z)\Big), \tag{7}$$

$$\sigma_{xz}'(x,y,z) = \Omega\Big(b_{xz}\Big(\sigma_{zz}'(z) + P_f(z)\Big) - P_f(z)\Big), \tag{8}$$

$$\sigma_{yz}'(x,y,z) = \Omega\Big(b_{yz}\Big(\sigma_{zz}'(z) + P_f(z)\Big) - P_f(z)\Big), \tag{9}$$

where (b_{ij}) is a normalized tensor constrained by the orientation of σ_1, and by ϕ and $\mathcal{R}_0$, and where Ω is a depth-dependent analytical function used to taper deviatoric stresses at the brittle-ductile transition below 50 km as:

$$\Omega = \max(0, \min(1, 1 + (z + 50{,}000 \text{ m})/150{,}000 \text{ m}). \tag{10}$$

We perform a slip tendency analysis for dynamic rupture simulations following Palgunadi et al. (2020), for which no dynamic rupture simulations are required. We vary the three angles constraining the orientation of σ_1 and compute the variable on-fault prestress and the closeness to failure, which are both modulated by the complex slab geometry. We find that a prestress, optimally oriented for a fault of azimuth 280° and dip 20° for pure thrust (rake 90°) faulting (i.e., σ_1 plunging 10° trenchwards) results in a close to critical prestress on the modeled megathrust

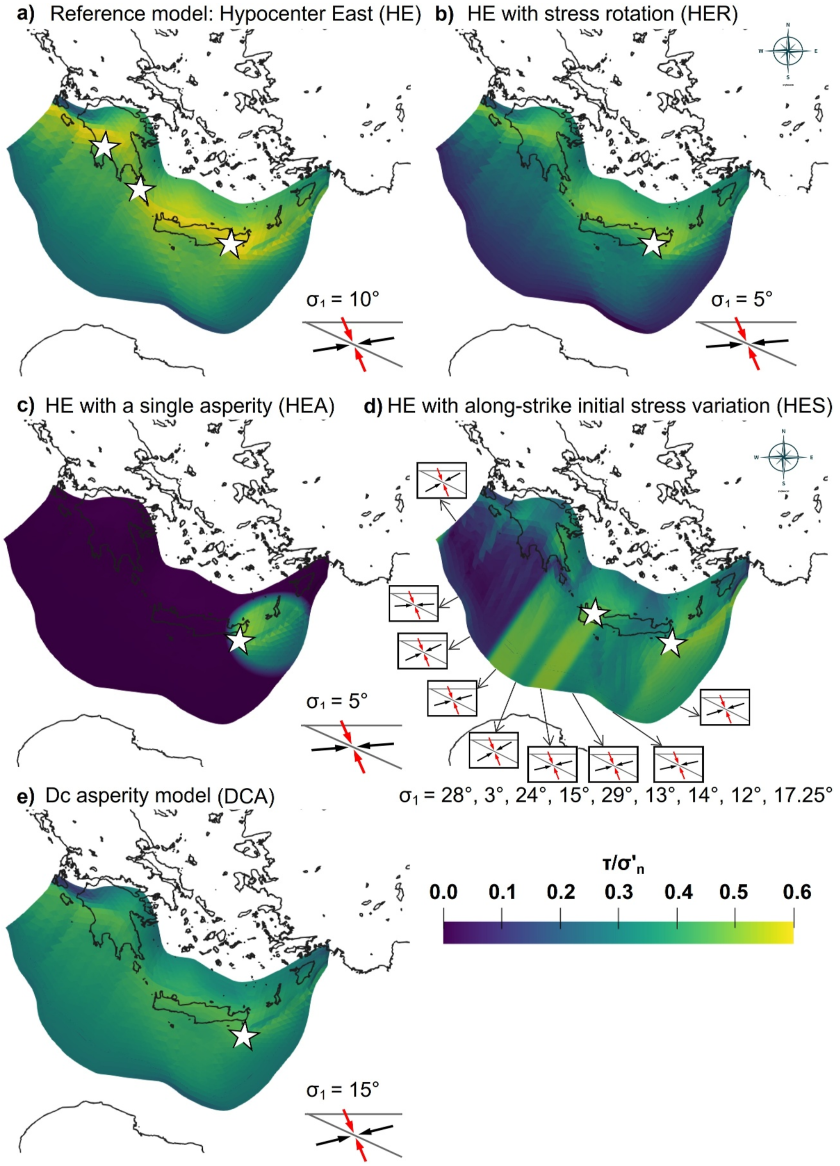

Figure 2. Ratio of initial shear stress (τ) to effective normal stress $\left(\sigma_n'\right)$ illustrating closeness to failure prior dynamic rupture onset. In our linear slip-weakening friction framework, frictional failure occurs when $\frac{\tau}{\sigma_n'} = 0.6 = \mu_s$. We here show $\frac{\tau}{\sigma_n'}$ for: (a) the reference model setup with Eastern (HE), Central (HM), and Western (HW) hypocenters, and the model allowing for off-fault plasticity (HEP). In all of these models, the fault is close to optimally prestressed, which can lead to margin-wide earthquake scenarios of $M_W \sim 9.0$. The bottom-right inset illustrates the plunge of the maximum (σ_1, black, 10°) and minimum (σ_3, red) principal stresses; (b) the rotated stress model (HER), characterized by a slightly shallower σ_1 plunge (5°). Here, the shallower fault portion is less optimally prestressed, which prevents shallow rupture, resulting in a dynamic rupture scenario of $M_W \sim 8.9$; (c) the single-asperity model (HEA) for a dynamic rupture earthquake scenario resembling the 1303 Crete earthquake, described in Section 3.2; (d) the segmented prestress model (HES, DCAS) informed by the regional stress inversion of Kkallas et al. (2021) described in Section 3.3. (e) the D_c-asperity model (DCA), characterized by a slightly steeper σ_1 plunge (15°). Here, the deeper fault portion is less optimally prestressed.

around the hypocenter depth when assuming $\mu_s = 0.6$. We apply these variables to all 10 dynamic rupture scenarios (Table 1 and Figure 2).

Finally, we assume a high pore-fluid pressure of 97% of the lithostatic load, which results in low effective normal stress σ_n', and realistic slip amplitudes, in line with dynamic rupture simulations of the 2004 Sumatra-Andaman earthquake (Madden et al., 2022).

Table 1
Dynamic Rupture Parameters Common to All Ten Models

Parameter	Value
Static friction coefficient (μ_s)	0.6
Dynamic friction coefficient (μ_d)	depth-dependent, 1.2–0.3
Critical slip distance (D_c) [m]	1.0
Maximum relative prestress ratio $(\mathcal{R}_0)$	0.7
Pore fluid pressure ratio (γ)	0.97
Stress shape ratio (Φ)	0.4
Dip of optimally oriented fault segments in reference prestress model [°]	20
Plunge of σ_1 in reference prestress model [°]	10
Plunge of σ_1 in model HER [°]	5
Plunge of σ_1 in models HES and DCAS [°]	3–29
σ_2 in Reference prestress model	horizontal in along-strike direction
Plunge of σ_3 in Reference prestress model [°]	−80
Seismogenic depth [km]	~15–43.3[a]

Note. The names of the models are defined in Figure 2 and in Sections 1 and 3. [a]see Figure 3.

2.3. Depth-Dependent Fault Friction and Rupture Nucleation

All fault-friction parameters are summarized in Table 1. We account for variations in frictional behavior with depth by using a depth-dependent μ_d and constant $\mu_s = 0.6$ leading to a depth-dependent frictional strength drop and realistic static frictional strength (Byerlee & Summers, 1976; E. Tinti et al., 2021). We follow (Scala et al., 2020; Shaw & Jackson, 2010; Vernant et al., 2014) and consider the seismogenic zone to range from ~15 km depth to ~40–50 km depth. Deformation of the uppermost 15 km is assumed to be dominantly aseismic aligned with the HASZ's relatively high convergence rate and low seismicity. We incorporate these constraints in our dynamic rupture models by assuming a slip-strengthening frictional behavior in the uppermost 15 km ($\mu_s = 0.6$ and $\mu_d = 1.2$, Figure 3). Slip-strengthening is a linear-slip weakening friction proxy (e.g., Ramos et al., 2021) for shallow velocity-strengthening behavior characterizing aseismic behavior (Scala et al., 2020; Shaw & Jackson, 2010; Vernant et al., 2014). Between 15 and 40 km depth, we use a lower $\mu_d = 0.3$, resulting in linear slip-weakening behavior. Between 40 and 50 km depth, we linearly increase μ_d from 0.3 to 1.2 resulting in slip-strengthening frictional behavior at depths deeper than 43.3 km. We assume constant $\mu_d = 1.2$ below 50 km depth.

We smoothly initiate all dynamic rupture scenarios within a spherical region surrounding the respectively assumed hypocenter location (Figure 2) by locally reducing the effective friction coefficient from its static to its dynamic value over 0.5 s at smoothly varying speeds with a maximum speed of 2,660 m/s, following Harris et al. (2018).

2.4. Off-Fault Plasticity

In model HEP, we analyze the effects of weak off-slab sediments co-seismically deforming. To this end, we consider a non-associative (visco-) plastic Drucker-Prager rheology (Andrews, 2005; Wollherr et al., 2018). The Hellenic Arc is characterized by relatively weak and unconsolidated sediments in the upper 15 km (Bohnhoff et al., 2001; Casten & Snopek, 2006; Jongsma, 1977; Le Pichon & Angelier, 1981; Pichon & Angelier, 1979; Shaw & Jackson, 2010; Taymaz et al., 1990).

The bulk material's friction coefficient ν is set to 0.6 and the bulk cohesion $C(z)$ varies with depth (Figure 3a):

$$C(z) = C_0 + C_1(z)\sigma'_{zz}. \tag{11}$$

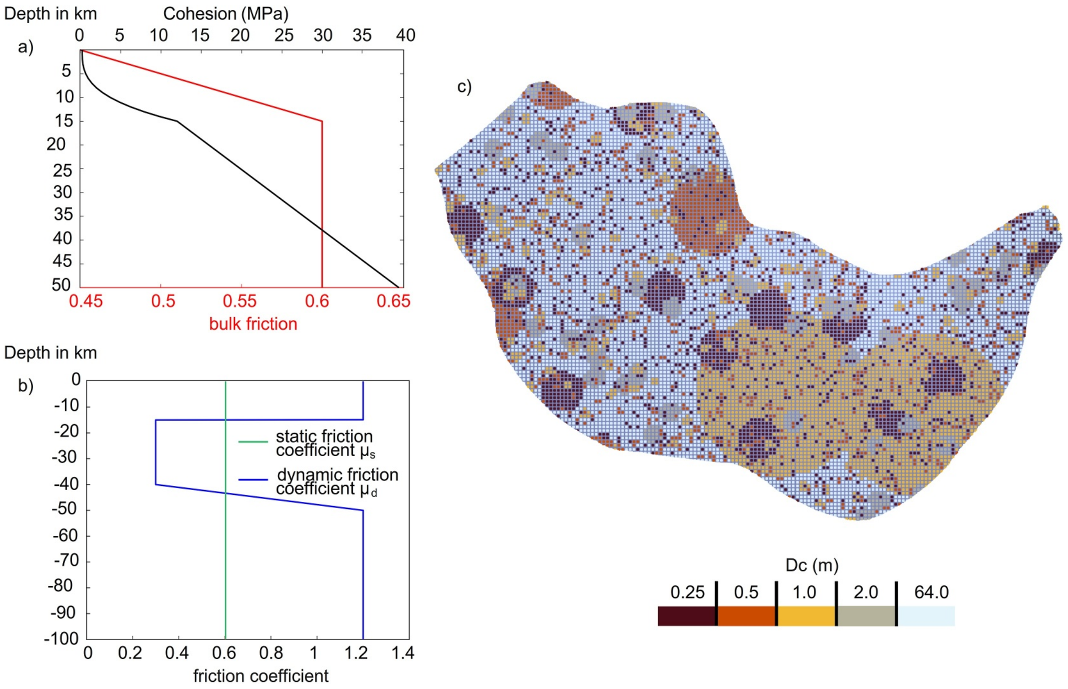

Figure 3. (a) Depth-dependent plastic cohesion and bulk friction for model HEP with off-fault plasticity. (b) Depth-dependence of friction coefficients in all models. We assume a constant static friction coefficient μ_s, while the dynamic friction coefficient μ_d varies with depth. Slip-strengthening $(\mu_d > \mu_s)$ is assumed in the upper 15 km and at depths lower than 43.3 km, and slip-weakening $(\mu_d < \mu_s)$ is assumed within the seismogenic zone. (c) Multiscale asperity models, with scale-dependent critical slip-weakening distance (D_c), following Ide and Aochi (2005) and described in Section 3.4.

$C_0 = 0.3$ MPa is a constant term that controls the amplitude and location of the off-fault yielding at shallow depth, while $C_1(z)$ is a depth-dependent term defining rock hardening, σ'_{zz} is the effective lithostatic stress. We use a viscoelastic relaxation time of $T_v = 0.03$ s. The off-fault plastic strain (Ma, 2008a) is quantified as

$$\eta(t) = \int_0^t \sqrt{\frac{1}{2}\dot{\epsilon}^p_{i,j}\dot{\epsilon}^p_{i,j}}. \tag{12}$$

A fully elastic rheology is considered in all other 9 models besides HEP.

3. Increasingly Complex Initial Conditions

In the following, we describe dynamic rupture model setups, which successively increase complexity based on the reference prestress and fault strength parameterization to account for smaller-scale megathrust heterogeneity.

All prestress initial conditions in our models are based on available seismic observations and a few trial-and-error dynamic rupture simulations. We use stress inversion results to generate our regionally varying initial stress setup. This enables constraining realistic initial conditions for dynamic rupture simulations without relying on geodetic locking models, which have been successfully used to initialize dynamic rupture scenarios (Chan et al., 2023; Ramos & Huang, 2019; Yang et al., 2019) but are difficult to obtain for offshore regions.

However, this reference prestress state remains relatively homogeneous. Various additional ingredients may be invoked to capture additional smaller scale heterogeneities, including prescribed stress asperities and barriers (Miyatake, 1992; Shibazaki & Matsu'ura, 1992; Dalguer et al., 2008; Cocco et al., 2016) (computationally challenging) fault roughness (Bartolomeo et al., 2010; Taufiqurrahman et al., 2022), or velocity-strengthening regions (Kaneko et al., 2010).

In this study, we explore the role of large stress asperities, along-strike segmented prestress, multi-scale frictional strength asperities.

3.1. Reference Laterally Homogeneous Prestress and Friction Parameters

Our reference model setup (HE) is based on a laterally homogeneous prestress setup with σ_1 dipping at 10° (Figures 2a and Table 1). All other parameters are set as described in Section 2. The model's rheology is purely elastic. In this reference model setup, we vary the epicentral location along the Hellenic Arc to investigate the influence of epicentral location on shallow slip, keeping the initial conditions constant and homogeneous. In the next step, we add off-fault plastic yielding to the reference model, maintaining the same homogeneous initial on-fault stress conditions.

3.2. Single-Asperity Prestress Model (HEA)

Our single-asperity model (HEA) earthquake scenario resembles the 1303 Crete tsunamigenic earthquake. We limit the potential rupture size by reducing the initial loading outside a circular predefined region, a prestress asperity. A laterally homogeneous stress setup is applied within this asperity, with a constant prestress ratio of $\mathcal{R}_0 = 0.7$. Outside, the shear stress is smoothly tapered over 35 km away from the asperity by linearly decreasing the shear stress until it reaches a value that equals the lithostatic stress.

Aiming to dynamically model a $M_W \sim 8$ earthquake, we choose an asperity size of radius 180 km based on the subduction-specific earthquake scaling relationship of Strasser et al. (2010), and consistent with earlier studies of the 1303 event (e.g., S. Tinti et al., 2005) (Figure 2c). We use σ_1 plunging 5° (an optimally prestressed fault would be oriented with a strike of 290° and dipping at 25°). We consider four possible epicenter locations, constrained from Papazachos et al. (1999); Papadopoulos et al. (2012); Yolsal-Çevikbilen and Taymaz (2012); Necmioğlu and Özel (2014), respectively, and three different prestress settings, based on Papadopoulos et al. (2012); Yolsal-Çevikbilen and Taymaz (2012); Necmioğlu and Özel (2014) by changing $Sh_{\max}$ accordingly. The laterally homogeneous stress is defined as in a), but we vary the orientation of principal stresses.

Of these 12 epicenter-prestress combinations, only three lead to spontaneous dynamic rupture propagation: (a) the epicenter and stress setup by Necmioğlu and Özel (2014); (b) the epicenter location proposed by Papadopoulos et al. (2012) in combination with the stress orientations inferred by Necmioğlu and Özel (2014); and (c) the epicenter location from Necmioğlu and Özel (2014) together with the initial stress setup from Papazachos and Nolet (1997). Our preferred scenario is (d) since it best reproduces the 1303 Crete earthquake in terms of dynamic rupture extent and moment magnitude.

3.3. Segmented Stress Models (HMS and HES)

In models HMS and HES, we assign along-arc varying initial stresses based on the stress inversion of Kkallas et al. (2021). We include only the stress values inferred from focal mechanisms (Kkallas et al., 2021) that contain a dominant thrust component. This leads to principal stress variations of σ_1 between 3° and 29° across the here assumed segments. The change of σ_1 influences how well the shallow or deep fault is prestressed and how close the segments are to failure.

We divide our HASZ modeling domain into nine seismotectonically homogeneous regions along an NW to SE axis and constrain the principal stress orientations for each area based on the stress inversion results. We smooth out sharp prestress discontinuities at the boundaries between sub-regions by applying a 2-D Gaussian smoothing kernel with standard deviation $\sigma = 3$ across the ∼2–4 km sampled 2D rectilinear grid storing the stress parameters.

The resulting segmented prestress is shown in Figure 2d. The azimuth and plunge of the maximum principal stress σ_1 vary segment-wise along the margin. The north-western portion of the slab, being non-optimally oriented, resolves little shear stress, while the south-eastern part is closer to failure. Higher shear over effective normal stress ratio at shallow depths compared with the stress model of a) relates with locally steeper σ_1 plunges.

3.4. Multi-Scale Asperity Models (DCA and DCAS)

D_c asperities that act as barriers can evolve due to differences in the fluid content of the subducted slab material, or coincide with fault roughness, or subducted seamounts (Bassett & Watts, 2015; Molina-Ormazabal et al., 2023). In models DCA and DCAS, we apply randomly distributed circular asperities with scale-dependent critical slip weakening distance (D_c) and fractal size-distribution, resulting in fewer larger than smaller-sized asperities (Figure 3). This multi-asperity model is adopted from Ide and Aochi (2005). To allow for sustained, realistic rupture propagation under our prestress assumptions, we adopt the following parameterization for the HASZ: D_c varies between 0.25, 0.5, 1, and 2 m. We chose $D_c = 1.0$ m within the largest asperity, which is consistent with the D_c value of all other scenarios with constant D_c. Smaller asperities may superimpose the larger ones. Consistent with Ide and Aochi (2005), we chose a background value of $D_c = 64$ m outside the asperities to limit rupture propagation. We note that other forms of heterogeneity may act as barriers, such as smaller-scale heterogeneity in prestress, static or dynamic friction coefficients, scale-dependent fracture energy, or geometric complexity (e.g., Gabriel et al., 2024; Ke et al., 2018; Ke et al., 2022; Wei et al., 2024; Weng & Ampuero, 2019; Wesnousky, 2006).

Our DCA model combines these multi-scale asperities with a steeper dipping σ_1 compared to the reference laterally homogeneous stress setup (Figure 2 and Section 3.1). The steeper plunge of σ_1 is necessary to facilitate sustained dynamic rupture propagation, given the locally increased fracture energy due to the heterogeneous Dc. Our model DCAS combines the multi-scale asperities with the segmented stress loading (Section 3.3), leading to the most heterogeneous initial conditions of all models studied in this work.

4. Results

4.1. Margin-Wide 3D Dynamic Rupture Scenarios

We present five models loaded by a laterally homogeneous Cartesian prestress tensor (Figures 2a, 2b, and 4). Four of these models explore "counterfactual" scenarios based on margin-wide dynamic rupture earthquake simulations and their sensitivity to epicenter location, prestress orientation, and off-fault plasticity.

All margin-wide counterfactual rupture scenarios are based on laterally homogeneous initial stress conditions and reach $M_W \sim 9$ moment magnitude (Table 2). The fifth scenario illustrates the sensitivity of the potential for margin-wide dynamic rupture on prestress configuration. While rupture dynamics of margin-wide scenarios with different epicenter locations are comparable, including localized supershear transition at the exact same deep slab location beneath Western Greece, the further west the epicenter location, the higher the amount of shallow slip and the more pronounced the modeled localized near-trench uplift. Adding off-fault plastic yielding limits shallow on-fault slip by preventing slip from penetrating into the velocity-strengthening region. A five-degree more shallowly plunging σ_1 leads to spontaneous rupture arrest before crossing the complete margin and prevents shallow slip.

4.1.1. Reference Model With Laterally Homogeneous Prestress and Friction Parameters and Eastern Hypocenter (HE)

We prescribe the hypocenter of our reference model (HE) below southeast Crete at a depth of 30 km (Figure 4a). Little slip penetrates to the west and into the shallow slip-strengthening region. Dynamic rupture initiates as a circular crack, turning pulse-like and propagating unilaterally toward the west after ~60 s simulation time (Figure 5a and Animation S1). Localized, deep supershear rupture is observed at the deep and steeply dipping portion of the slab, at ~40 km depth around western Crete, and coincides with the area of the largest peak slip rate up to 6.9 m/s (Table 2). At the same depth (~40–45 km), the highest stress drop is observed (Figure 6). The slab interface changes from a relatively flat dipping portion of the slab to a much steeper dipping segment of the megathrust at this depth. This geometry change coincides with higher initial stresses (Figure 2). Large-scale megathrust geometry changes leading to deep, localized propagating supershear rupture have been reported previously in geodynamically constrained 2D and 3D megathrust dynamic rupture models (van Zelst et al., 2019; Wirp et al., 2021).

Dynamic rupture propagates west until reaching the prescribed north-western edge of the Hellenic Arc slab model, that is, yielding a margin-wide rupture scenario, after 150 s simulation time. The highest accumulated slip of ~11 m is modeled below southwest Crete. The resulting vertical seafloor displacement distribution reflects the distribution of fault slip. Uplift of up to 1.6 m is modeled south of Crete and southwest of Peloponnese. Subsidence of ~1 m can be observed north of Crete, on Peloponnese, and across the islands of Zakynthos and Kefalonia (Figure 4a).

4.1.2. Models With Different Hypocenter Locations (HM and HW)

We vary epicentral locations to investigate the effect of rupture propagation direction on rupture dynamics, slip distribution and extent, and seafloor displacements. We present two models, one with its epicenter located

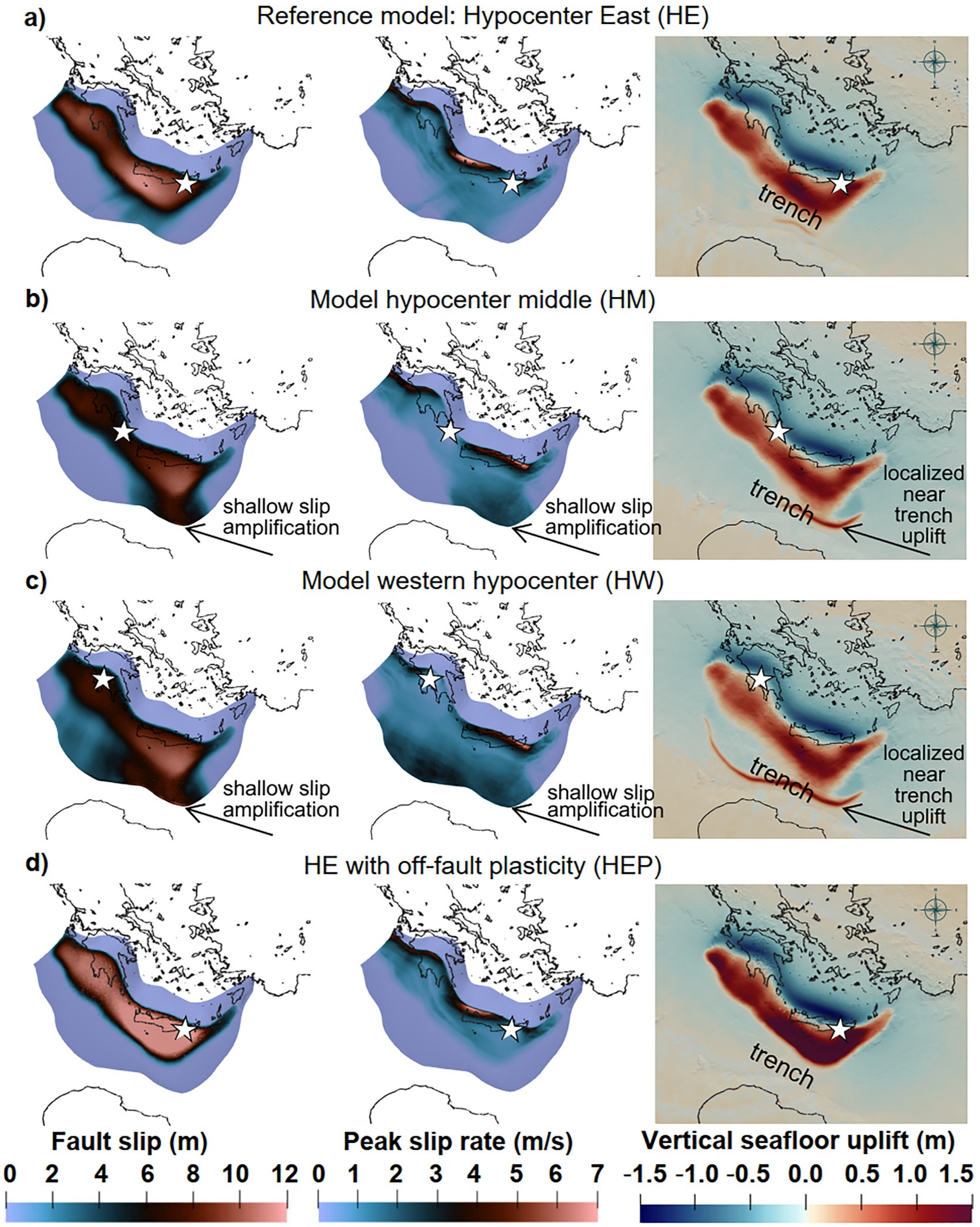

Figure 4. Rupture characteristics of modeled counterfactual margin-wide 3D dynamic rupture scenarios HE, HM, HW, and HEP: Fault slip ([m], left), peak slip rate ([m/s], middle), and vertical seafloor uplift ([m], right) distributions. Changing the hypocenter location (white star) in (a), (b), and (c) impacts shallow fault slip, generating localized near-trench uplift visible in the vertical seafloor displacements (right). We account for the possibility of off-fault plasticity in model HEP (d)), extending the eastern hypocenter reference (HE) scenario in (a). This restricts slip to the deeper fault areas but generates increased slip amplitudes, which, combined with off-fault plastic strain, increases vertical seafloor displacements. The color scales are saturated. See Table 2 for absolute maximum values. See Animations S1-S4 for illustrations of slip rate evolution across the megathrust.

between Crete and Peloponnese (middle hypocenter model, HM), and one with an epicenter located further west, below northwest Greece (western hypocenter model, HW). Both have the same epicentral depth of ∼30 km as model HE.

Table 2
Rupture Characteristics for All 10 Dynamic Rupture Simulations

Model description	ASl[a][m]	PSR[b][m/s]	V_r[c][m/s]	Disp.[d][m]	M_W[e]
Reference model: hypocenter east (HE)	11.323	8.600	3,248	1.642	9.04
Model hypocenter middle (HM)	12.974	6.974	3,003	1.504	9.06
Model hypocenter west (HW)	15.501	8.207	2,900	1.477	9.12
HE with off-fault plasticity (HEP)	22.125	7.084	3,297	2.913	9.13
HE with rotated stress (HER)	6.239	5.108	2,859	1.625	8.61
HE with single asperity (HEA)	4.963	2.205	2,374	1.288	8.04
HM with along-strike initial stress variations (HMS)	12.175	4.819	2,585	1.708	8.81
HE with along-strike initial stress variations (HES)	5.244	1.829	1,631	1.171	8.12
D_c-asperity model (DCA)	13.768	33.044	3,138	3.492	8.42
DCA with along-strike initial stress variations (DCAS)	2.626	2.355	2,185	0.557	7.52

[a]Fault slip. [b]Peak slip rate. [c]Rupture velocity. [d]Displacement. [e]Moment magnitude.

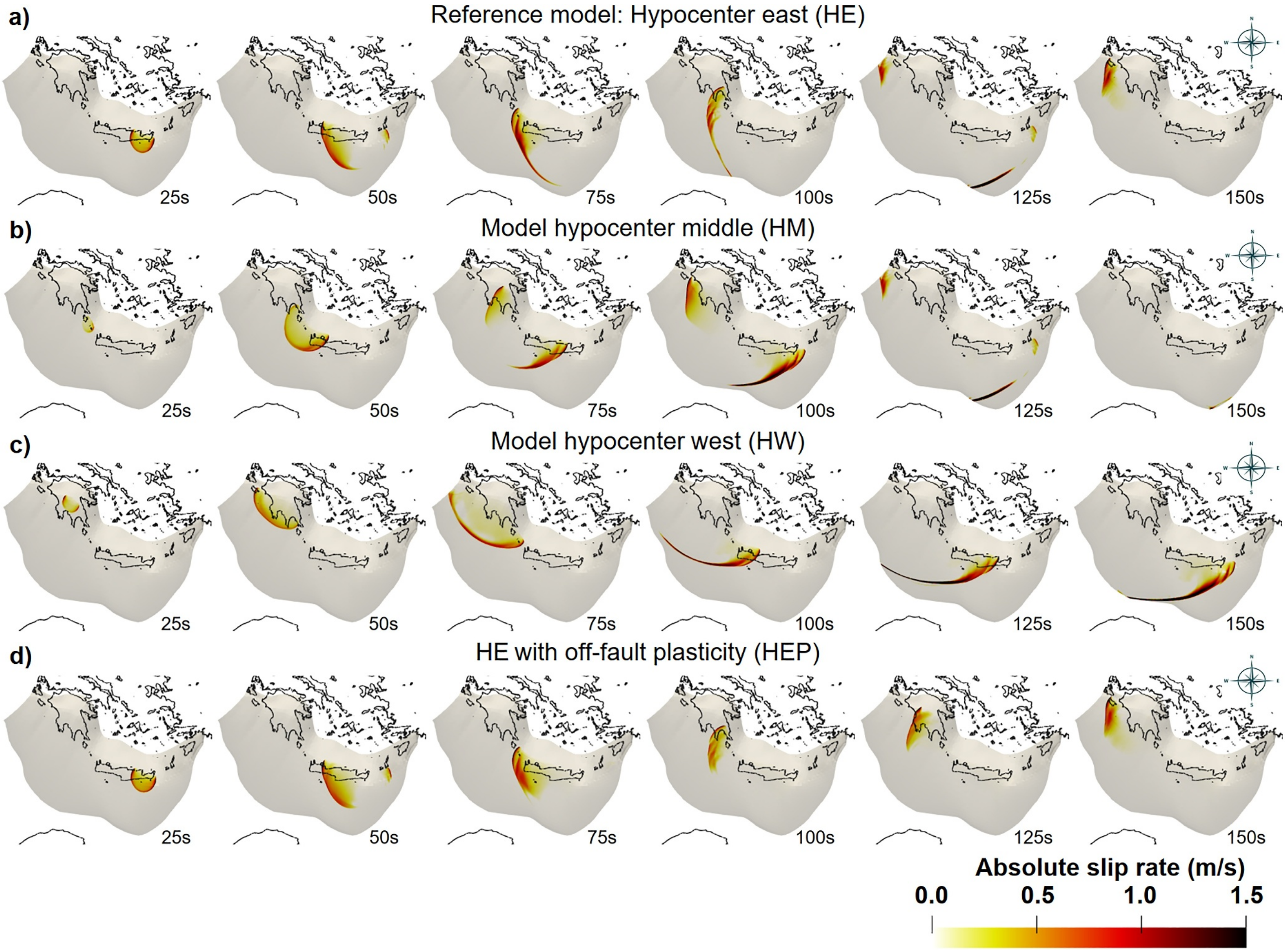

Figure 5. Slip rate evolution of four margin-wide rupture scenarios: Absolute slip rate [m/s] after 25, 50, 75, 100, 125, and 150 s simulation time (Movies S1–S4): (a) Reference scenario: Hypocenter East (HE), (b) Hypocenter Middle (HM), (c) Hypocenter West (HW), and (d) Hypocenter East with off-fault Plasticity (HEP) scenarios. The color scale is saturated. For absolute maximum slip rate values see Table 2.

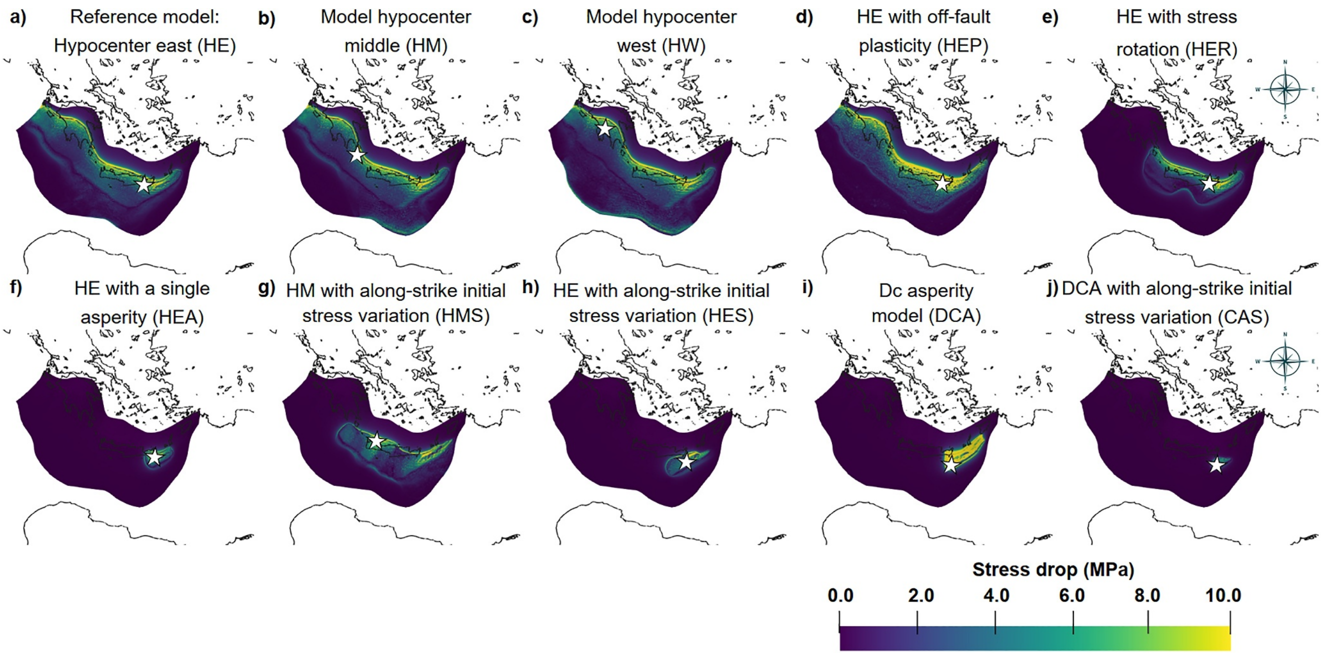

Figure 6. Stress drop of the ten dynamic rupture scenarios presented in this study: (a)–(c) Margin-wide dynamic rupture scenarios based on laterally homogeneous initial stress conditions (HE, HM, HW), (d) HEP dynamic rupture scenario incorporating off-fault plastic yielding, (e) HER model with a less steeply dipping maximum principal stress σ_1 than in HE (HER), (f) single-asperity model (HEA), (g) and (h) segmented stress models (HMS and HES), (i) multiscale asperity model based on the reference laterally homogeneous stress (DCA), and (j) multiscale asperity model based on the segmented stress model (DCAS). The highest stress drop for (a)–(e) can be observed near the slab's deep, steeper dipping edge. In (g), the stress drop is highly inhomogeneous and follows the heterogeneous initial stress conditions (Figure 2). For (i), the stress drop is particularly high, compared to the other models. A closeup of (f), (h), and (j) can be found in Appendix Figure B2. We measure stress drop as the difference in fault stress before and after dynamic rupture. We caution that shallow rupture propagation into the slip-strengthening region of the slab, which is associated with small or negative stress drops, appears as locally apparently elevated stress drops.

In the scenario with a middle hypocenter (HM), we observe initial circular crack-like rupture followed by bilateral pulse-like rupture propagation toward the east and the west after the updip rupture front reached the shallow velocity-strengthening region (Figure 5b and Animation S2). Supershear transition occurs at around 50 s simulation time at the same deeper, steeply dipping portion of the slab close to western Crete as in model HE. However, supershear rupture is, in this scenario, initiated by a SE propagating rupture front. The location of supershear rupture onset again coincides with the maximum PSR in this model, reaching ∼6.1 m/s, and high local stress drop.

In the western hypocenter scenario (HW), we observe similar but mirrored rupture dynamics compared to model HE, resulting in unilateral eastward pulse-like rupture propagation. Localized supershear transition occurs at a later stage of the simulation, at around ∼100 s simulation time (Figure 5c and Animation S3) when rupture reaches the deep slab beneath western Crete at ∼45–50 km depth. Supershear transition coincides with the model's maximum PSR of ∼8.2 m. Despite the overall similar earthquake characteristics, in model HW we observe a wide, localized area of shallow slip to the trench, reaching up to 10 m in amplitude and driven by shallow peak slip rates of ∼3–4 m/s.

Cases HE, HM, and HW all result in margin-wide rupture. In all of these models with varying epicentral locations, the rupture front penetrates into the shallow slip-strengthening fault region after ∼100 s simulation time, respectively. Importantly, the further west the epicentral location, the higher the amount of shallow slip. Rupture propagation into the shallow slip-strengthening region of the fault is more pronounced for models HM and HW, evidenced by the high slip rate in the shallow part, and results in an additional localized near trench seafloor uplift (Figure 4). Variations between the models are solely due to dynamic rupture evolution and rupture directivity.

For all three scenarios, the maximum slip is resulting at the center of the megathrust, below Crete, within the deeper slip-weakening region (Figure 4). With a high accumulated slip of ∼11.3 m (HE), ∼13.0 m (HM), and ∼15.5 m

(HW), the models produce comparable maximum vertical seafloor displacement of 1.64 m (HE), 1.50 m (HM) and 1.48 m (HW), respectively.

The stress drop for models HM and HW resemble the stress drop of the HE model, with some differences at shallow depths, where HM and HW display apparently high stress drop locally. The stress drop is measured as the difference in fault stress before and after the earthquake in the dynamic rupture simulations as

$$\sqrt{T_s^2 - T_d^2}, \tag{13}$$

with T_s and T_d being the shear stress changes in strike and dip direction. Consequently, shallow rupture propagation into the slip-strengthening region of the slab (Figure 6), which is associated with locally small or negative stress drops, appears as, apparently elevated stress drops. While shallow stress drop is not high in absolute terms, it contrasts with the absence of stress drop observed in model HE, associated with the absence of shallow rupture propagation. For all three models (HE, HM, and HW), the highest stress drop is observed near the slab's deep, steeper dipping edge, which may explain deep high-frequency radiation as observed for the Tohoku-Oki earthquake (e.g., L. Meng et al., 2011; Galvez et al., 2014).

The seafloor uplift, that is, the vertical seafloor displacement distribution, produced by models HM and HW resembles the uplift of the HE scenario (Figure 4), except for localized near-trench uplift, produced by shallow slip. The further west the epicenter, the more pronounced and elongated the modeled localized near-trench uplift.

4.1.3. The Role of Off-Fault Plasticity (Model HEP)

We add off-fault plastic yielding to the reference scenario (HE) to investigate the role of unconsolidated sediments in the dynamically evolving slip and seafloor displacements. Our dynamic rupture models show that considering 15 km of relatively unconsolidated sediments that deform co-seismically can significantly enhance the amount of uplift. Off-fault plastic yielding is most pronounced at shallow depths and within the hanging wall of the megathrust (Figure 7). Off-fault deformation forms a characteristic flower structure at shallow depth. The distribution of the off-fault plastic deformation follows the fault geometry and uplift patterns in Figure 4d. Vertical seafloor uplift is now reaching ∼3 m (Figure 4d), which is double compared to the elastic scenario HE.

Both the maximum rupture speed, V_r, and the peak slip rate, PSR, are expected to be limited in dynamic rupture simulations with off-fault plasticity (e.g., Andrews, 2005; Dunham et al., 2011; Gabriel et al., 2013). However, we observe that the average rupture velocity is not reduced in model HEP compared to model HE. In distinction, PSR is ∼1.5 m/s, which is lower than in model HE. Thus, while we do observe lower PSR when allowing for off-fault plasticity, the average rupture speed remains comparable. We note that our choice of $\mathcal{R}_0 = 0.7$ implies that the S ratio of initial strength excess to nominal stress drop (Das & Aki, 1977) of models HEP and HE is with $S = 0.43$ lower than values explored in previous studies.

Off-fault plastic yielding limits shallow on-fault slip, as observed in 3D dynamic rupture scenarios of the 2,004 Sumatra megathrust event (Ulrich et al., 2022) and for low-angle normal faults (Biemiller et al., 2023; Kim & Sanderson, 2006). Shallow slip within the slip-strengthening region is efficiently prevented (Figure 4d).

The maximum on-fault slip is ∼10 m larger than in the purely elastic scenario HE, while the moment magnitudes of both scenarios are comparable (Table 2). Localized supershear transition after 100 s simulation time is persistent (Animation S4). The highest PSR of ∼7 m/s is modeled on the deep, steeply dipping portion of the slab, where the highest stress drop is observed (Figure 6).

4.1.4. Shallowly Plunging σ_1 (Model HER) Prevents Margin-Wide Rupture and Shallow Slip

In scenario HER, we assume that σ_1 plunges at 5°, which is slightly less than in the HE reference scenario, which assumes a σ_1 plunge of 10°. Such shallowly plunging σ_1 leads to an increase in the ratio of initial shear stress τ over effective normal stress σ_n on the deeper portions of the slab (Figure 2b) and a decrease at shallower depths. We do not account for a potential depth-dependence of σ_1. Kkallas et al. (2021) divide the stress regime of the Hellenic arc seismogenic zone into segments of 0–30 km and 30–60 m depth, which could be explored in future models. Similarly to the model allowing for off-fault plasticity (HEP), dynamic rupture propagation in model HER remains limited to the deeper megathrust. The maximum slip is located below Crete and is 5–9.3 m lower

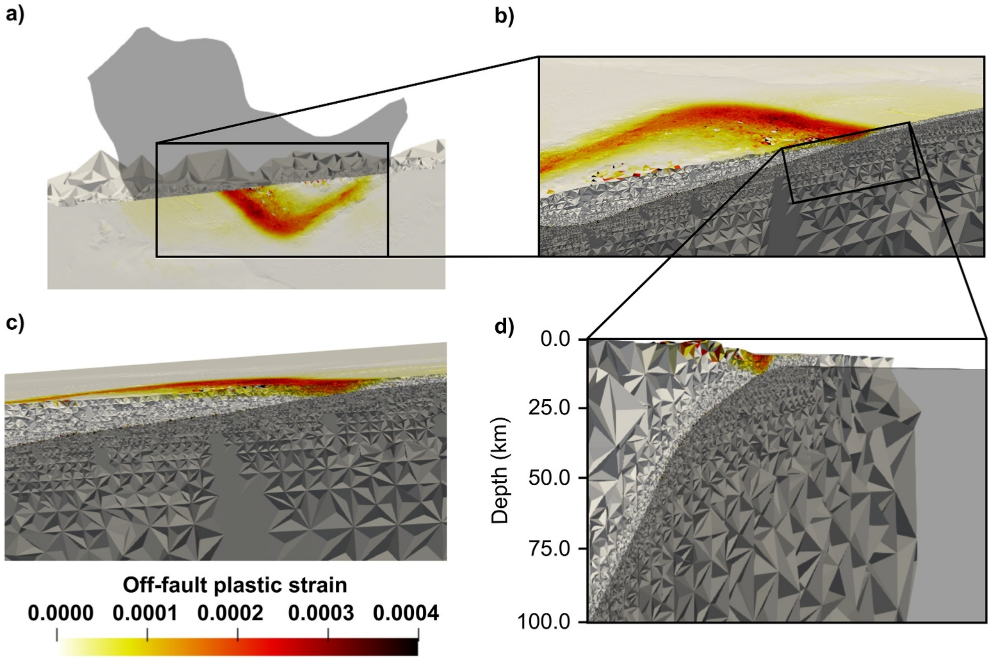

Figure 7. Accumulated off-fault plastic strain quantified as η in scenario HEP (Section 2.4): (a) Map view of the fault and free surface showing η and the location of the cutting plane used for the vertical slice in (b), (c) and (d). (b) Close-up cut-away view combining a map view and a vertical slice through the damage zone. The megathrust interface is transparent dark gray. η is displayed from above and on the cutting plane. (c) Same as in (b), but from another viewing direction. (d) Cut-away view from NW combining the megathrust interface, displayed as transparent dark gray, and a vertical slice showing η. The unstructured tetrahedral mesh is refined around the slab and coarsens with distance.

than in the margin-wide rupture models HE, HM, and HM (Table 2 and Figure 8). This results in a smaller moment magnitude of $M_W \sim 8.6$. In this model, neither supershear rupture transition nor rupture propagation into the shallow slip-strengthening region is observed (Figure 9d). Dynamic rupture spontaneously arrests in the west. The stress drop of model HER is highest at the deep, steeply dipping portion of the fault, similar to models HE, HM, HW, and HEP (Figure 6).

The maximum seafloor uplift southeast of Crete is ~1.6 m, comparable to the reference model (HE). We observe notable differences between models HER and HE in the distribution of seafloor displacements (Figures 4 and 8). The uplift area in the HER model is much smaller and located solely south of Crete. A subsidence of ~0.5 m is observed north of Crete.

4.2. Single Prestress Asperity Model (HEA)

This model illustrates the effectiveness of prestress asperities in limiting the resulting moment magnitude and slip extent of dynamic rupture earthquake scenarios while simultaneously causing a relatively high seafloor displacement. We discuss the applicability of this approach to model the 1303 Crete earthquake in Section 5.2.

In the single asperity dynamic rupture scenario HEA, we taper shear stress from a laterally homogeneous stress tensor outside a circular region, which size is constrained by the earthquake scaling relationship of Strasser et al. (2010) as explained in Section 2.

In model HEA, dynamic rupture propagation stops after 50 s at the eastern edge of the asperity (Figure 9, and Animation S6) and does not propagate to shallow depths. The resulting fault slip and seafloor displacements are displayed in Figures 8b and B1a. This $M_W 8.0$ earthquake scenario causes a maximum fault slip of ~5 m, which is ~6 m less than in the reference model HE. It produces a vertical seafloor uplift of up to ~1.3 m located SE of Crete. Even though the lateral extent of the seafloor displacement is limited to a small area compared to the counterfactual margin-wide rupture scenarios HE, HM, and HW, the local peak uplift is only ~0.2–0.3 m smaller.

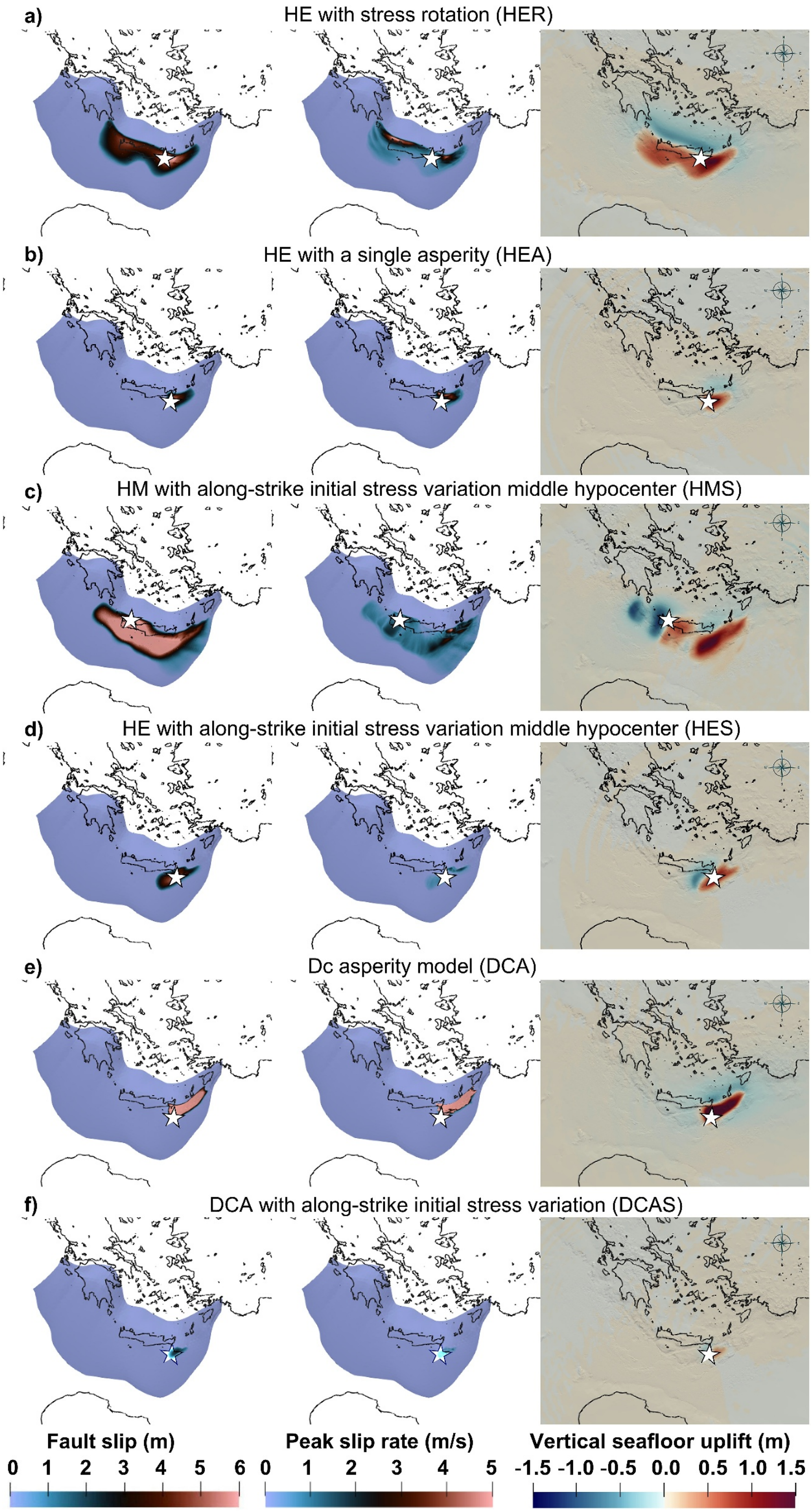
a)
HE with stress rotation (HER)
b)
HE with a single asperity (HEA)
c)
HM with along-strike initial stress variation middle hypocenter (HMS)
d)
HE with along-strike initial stress variation middle hypocenter (HES)
e)
Dc asperity model (DCA)
f)
DCA with along-strike initial stress variation (DCAS)
Fault slip (m)
0 1 2 3 4 5 6
Peak slip rate (m/s)
0 1 2 3 4 5
Vertical seafloor uplift (m)
-1.5 -1.0 -0.5 0.0 0.5 1.0 1.5

Figure 8.

The highest PSR of model HEA is observed at the deeper and steeply dipping portion of the slab (Figures 6f and B2a), similar to the margin-wide earthquake scenarios (HE, HM, and HW).

4.3. Dynamic Rupture Models With Along-Arc Segmented Prestress (Models HMS and HES)

We increase the complexity and realism of our dynamic rupture initial conditions by assuming a heterogeneous, along-arc segmented prestress. Under these conditions, we investigate how different epicentral locations lead to differences in rupture extent, peak slip rate, and absolute slip, resulting in remarkably different moment magnitudes, with higher PSR and M_W for a hypocenter located further west (HMS). Heterogeneities of the initial stress limit the fault slip extent and restrict rupture propagation to the deeper slip-weakening region of the slab. The segmentation in terms of initial stresses is reflected in the uplift pattern (HMS), which is much more complex than for the models with laterally homogeneous initial stress (HM).

Figures 8c, 8d and B1b present two dynamic rupture earthquake scenarios based on the along-strike highly variable, segmented prestress model constrained from stress inversion by Kkallas et al. (2021) (Figure 2 and Section 2). The HMS scenario (middle hypocenter) uses a hypocenter located below Chania in north-western Crete, while the HES scenario (eastern hypocenter) is based on a hypocenter located southeast of Crete. Both hypocenters are located within regions with a high ratio of initial shear over effective normal stress.

In the HMS scenario, rupture propagates bilaterally to both sides of the Hellenic Arc megathrust (Figures 9c and B3c, Animation S7). Large parts of the megathrust are ruptured. However, at shallow depths, rupture does not propagate into the slip-strengthening region across the complete margin but only near the shallow eastern edge of the slab (Figure 8c). The maximum fault slip is ∼12.2 m, which is comparable to the margin-wide rupture scenarios (HE, HM, and HW). High accumulated fault slip concentrates southwest of the island Kynthera and below western Crete, modulated by the shape of the megathrust. The highest PSR of ∼4.8 m/s is simulated southeast of Crete (Figure 8c) and aligns with the stress drop distribution, with areas of high stress drop experiencing high PSR (Figure 6).

The HMS scenario results in a maximum vertical seafloor uplift of ∼1.7 m southeast Crete and subsidence of ∼1 m close to western Crete and southwest of Peloponnese and the island Kynthera. This uplift is slightly higher than for the margin-wide rupture models HE, HM, and HW. The uplift pattern of the HMS model is much more complex than that of the other models. The along-arc segmented loading provokes two near trench uplift features east of the hypocenter, and two subsidence features west of the hypocenter. The HMS scenario moment magnitude is $M_W \sim 8.81$, which is slightly smaller than that of the counterfactual margin-wide scenarios.

The HES scenario ruptures a smaller area than the HMS scenario and leads to a smaller maximum slip of ∼5.2 m, southeast the Crete island (Figures 8d and B1b, Animation S8). This moment magnitude $M_W \sim 8.12$ earthquake causes a relatively small vertical seafloor uplift of ∼1.2 m. In this scenario, the rupture propagation stops after 50 s (Figure 9d) and does not penetrate into the shallow slip-strengthening region.

The absolute slip in model HMS is comparable to the counterfactual margin-wide rupture scenarios and ∼0.8 m smaller than in model HM. However, the maximum PSR of ∼4.8 m is with ∼2 m/s much smaller than in model HM. In contrast to HM, the highest PSR does not coincide with the deep and steeper dipping portion of the slab but represents the heterogeneous prestress distribution (Figure 2). The heterogeneity in the prestress of HMS results in a very different seafloor uplift compared to HM. No localized near trench uplift is observed. While the uplift in model HM follows the fault structure, with subsidence located north of it. In model HMS, the uplift is located east of the hypocenter location, while the subsidence is located west of the hypocenter, following the prestress segmentation.

Figure 8. Rupture characteristics for the six non-margin-wide spontaneously arresting dynamic scenarios: Fault slip [m], peak slip rate [m/s], and vertical displacement distribution for (a) model HER using a less steeply oriented maximum principal stress σ_1 than in HE, (b) the single-asperity model (HEA), (c) and (d) models HMS and HES based on a segmented stress model with two different epicenter locations, (e) the multiscale asperity model DCA using the reference laterally homogeneous stress and (f) the multi-scale asperity model DCAS using the segmented stress. White stars mark the respective hypocenters. Note the significant differences in fault slip across the scenarios and varying seafloor uplift patterns. The color scales are saturated. For absolute maximum values and other characteristics such as moment magnitudes, see Table 2. A closeup of (b), (d), and (f) is shown in Appendix Figures B1 and B4.

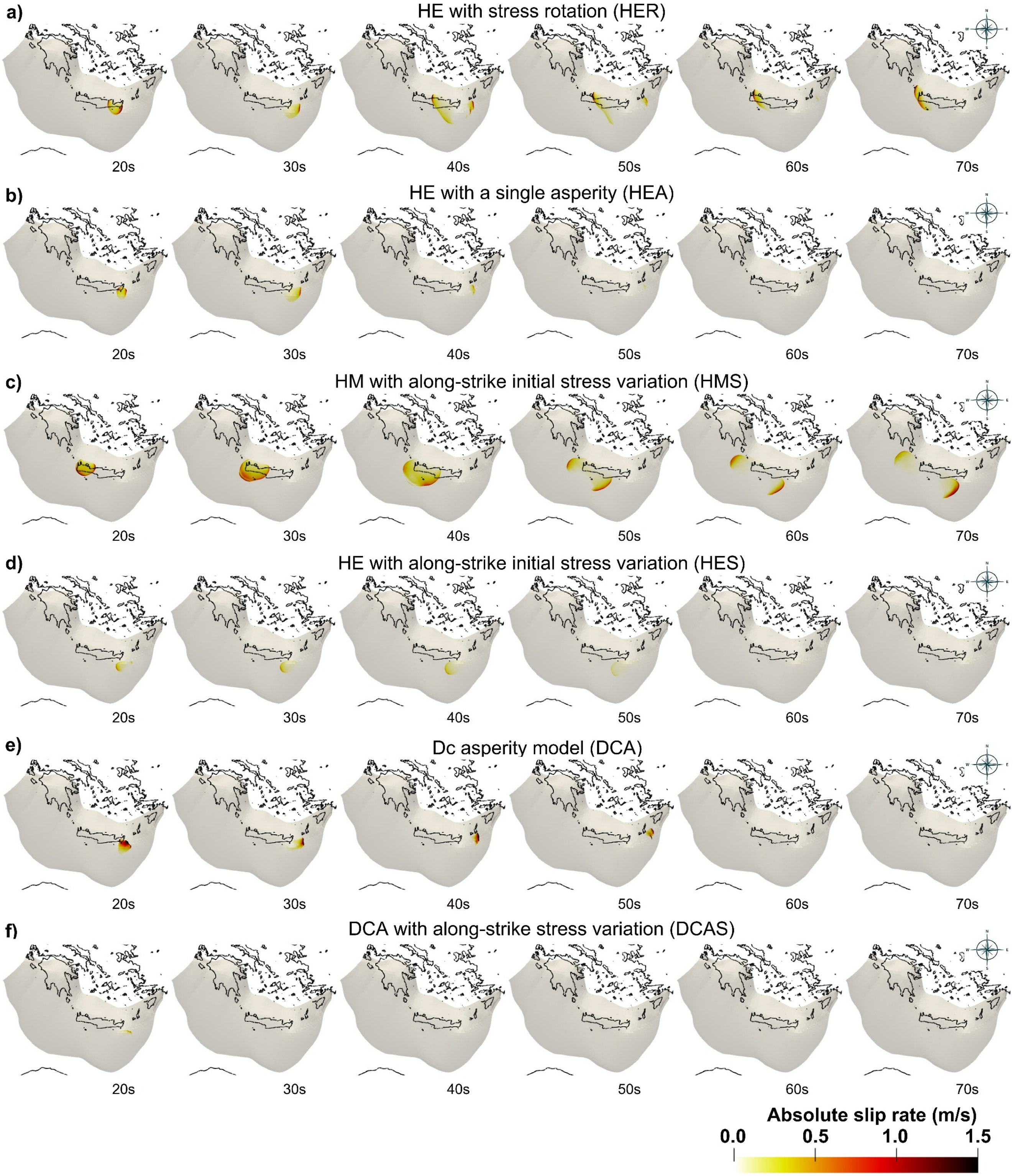
a)
HE with stress rotation (HER)
20s
30s
40s
50s
60s
70s
b)
HE with a single asperity (HEA)
20s
30s
40s
50s
60s
70s
c)
HM with along-strike initial stress variation (HMS)
20s
30s
40s
50s
60s
70s
d)
HE with along-strike initial stress variation (HES)
20s
30s
40s
50s
60s
70s
e)
Dc asperity model (DCA)
20s
30s
40s
50s
60s
70s
f)
DCA with along-strike stress variation (DCAS)
20s
30s
40s
50s
60s
70s
Absolute slip rate (m/s)
0.0
0.5
1.0
1.5

Figure 9.

4.4. Combining a Multi-Scale D_c-Asperity Model With Laterally Homogeneous Prestress (Model DCA)

Model DCA is characterized by a comparable maximum slip and rupture velocity to the counterfactual margin-wide rupture scenarios HE, HM, and HW, but a smaller M_W. With a ∼5-times higher PSR and highly heterogeneous rupture dynamics caused by the randomly distributed D_c-asperities on the slab, it results in vertical seafloor displacements of up to ∼3.5 m, which is more than double the amount of that of the M_W9 margin-wide rupture models.

In scenario DCA, we use the multi-scale asperity model (Section 3.4) in combination with laterally homogeneous prestress but a slightly steeper dipping σ_1 (plunge 15°) compared to the reference model HE (and in models HM, HW, HEP and HER). D_c can now locally be smaller or higher than in previous scenarios. Dynamic rupture is initiated within a large asperity with $D_c = 1$ m on the south-eastern part of the slab and propagates unilaterally toward the east (Figure 9e and Animation S9). Dynamic rupture arrests when propagating into slab areas combining low initial shear stresses and high D_c values.

Model DCA results in a $M_W \sim 8.42$ earthquake, with a maximum slip of ∼13.8 m (Table 2 and Figure 8e). The D_c-asperities induce strongly heterogeneous and locally high peak slip rates compared to the previously described non-margin-wide rupture scenarios. The stress drop is high throughout the ruptured area (Figure 6) and specifically higher than in model HE. Dynamic rupture stress drop variations are controlled mainly by the initial stress and the friction coefficients μ_s and μ_d but not by D_c, given that slip is locally, in general, exceeding D_c. Thus, DCA's higher stress drop is due to the steeper dipping σ_1 in this model (Figure 2).

Model DCA shows more heterogeneous dynamics than the previous models. The rupture front first propagates in the downdip direction toward the east (Figures 5e and B3e), then, while the rupture propagates along the fault strike, it splits up into two rupture fronts. In agreement with the analysis in Ide and Aochi (2005), dynamic rupture propagation governed by multi-scale D_c-asperities is complex, forming a cascade triggering asperities. Thus, forecasting earthquake characteristics solely based on its epicentral location is difficult.

The peak uplift of ∼3.5 m is significantly larger than for the HE scenario with homogeneous prestress and eastern hypocenter. The uplift area extends from southeast Crete to southeast of the island of Karpathos. This uplift is consistent with worst-case scenario assumptions made in regional tsunami studies (e.g., S. Tinti et al., 2005; Lorito et al., 2008).

4.5. Model Combining the Multi-Scale Asperity Model and the Segmented Stress Model (DCAS)

Combining heterogeneous prestress and frictional megathrust properties (D_c) lowers dynamic rupture fault slip, rupture extent, and moment magnitude due to effective barriers arising from the imposed asperities. The rupture propagation is highly heterogeneous, governed by the rupture front interacting with the D_c-asperities and being affected by changing stress conditions.

Our dynamic rupture scenario DCAS combines the multi-scale asperity model and the segmented stress model (see Section 2) to the most complex initial conditions among the 10 models. We use the same south-eastern epicentral location as in the DCA scenario. In model DCAS, rupture propagates eastward (Figure B2f) and splits into two rupture fronts, one propagating downdip and the other propagating along the fault strike direction. The rupture area is relatively small compared to model DCA or HES. In model HES, rupture propagates bilateral, while in DCA and DCAS, propagation is primarily unilateral toward the northeast. In both D_c-asperity models (DCA and DCAS), the random distribution of D_c-patches along the arc governs rupture propagation complexity. As the rupture front propagates, it triggers the D_c patches on the fault, which generates unpredictable and heterogeneous rupture propagation patterns (Ide & Aochi, 2005). The maximum fault slip in DCAS is with ∼2.6 m five times smaller than in the DCA model and half the amount of slip of HES (Table 2 and Figures 8f, B1c). The maximum PSR is a tenth of the PSR in model DCA and four times smaller than in the margin-wide rupture models

Figure 9. Slip rate [m/s] snapshots for the six non-margin-wide spontaneously arresting dynamic rupture scenarios (Movies S5–S10): (a) HER, based on a less steeply oriented maximum principal stress σ_1 than in HE, (b) HEA, the single prestress asperity model, (c) and (d) HMS and HES, combining along-arc heterogeneous, segmented prestress with two different hypocenter locations, (e) DCA, the multi-scale D_c-asperity model combined with the reference laterally homogeneous prestress and (f) DCAS, the multi-scale D_c-asperity model combined with along-arc heterogeneous prestress. Slip rates [m/s] are shown at 20, 30, 40, 50, 60 and 70 s simulation time. The rupture evolution model DCAS after 5, 10, 15, 20, and 25 s can be found in Appendix Figure B4. A closeup of the rupture evolution for all models at 20 s simulation time can be found in Appendix Figure B3.

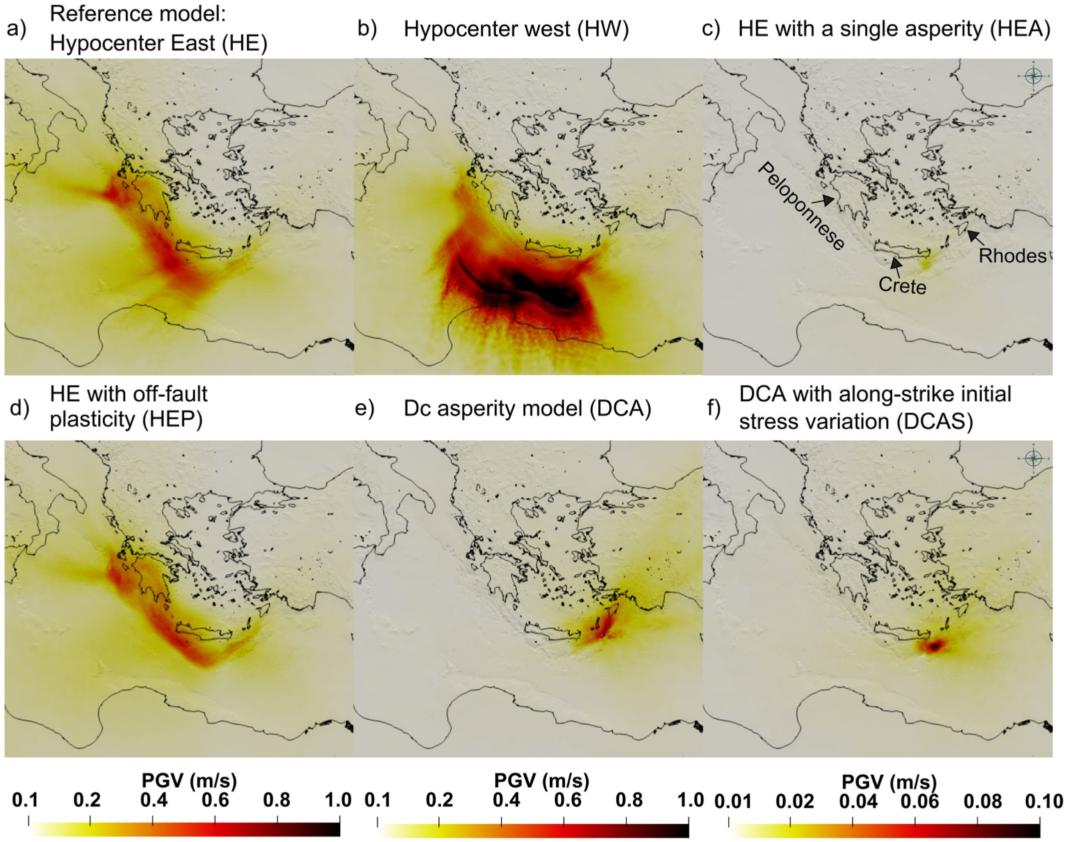

Figure 10. Horizontal peak ground velocities (PGVs) (resolved up to 2.7 Hz in the vicinity of the slab but with spatially decreasing accuracy away from it) for (a) Reference model (HE), (b) model with western hypocenter location (HW), (c) single stress-asperity model (HEA), (d) model including off-fault plastic yielding (HEP), (e) the model based on the multi-scale asperity model and the reference laterally homogeneous stress (DCA) and (f) the model based on the multi-scale asperity model and the segmented stress model (DCAS). Note the different scales for (c) and (f). In (a) (model HE), the highest PGV is located above the western Hellenic Arc. The PGV in (d) (model HEP) has a similar pattern but high PGVs (e.g., >0.5 m/s) affect a smaller area than in model HE. (b) (model HW) shows the highest PGVs (∼1.0 m/s) and also the largest spatial extent of high PGV values, with PGVs higher than 0.5 m/s extending up to the northern coast of Africa. Models HEA, DCA, and DCAS are characterized by locally smaller and more localized PGVs due to their smaller rupture extent (Figure 8) and moment magnitude (c) max. PGVs of model HEA ∼0.02 m/s, which is ∼2% of max. PGVs of model HW, (e) PGVs of model DCA, restricted to a small area east of Crete, (f) max. PGVs of model DCAS ∼0.06–0.2 m/s, which is ∼6%–20% of max. PGVs of model HW). The color scale is saturated. For absolute maximum values see Table 2.

(HE, HM, and HW). It is slightly higher than in model HES but comparable to the single asperity model (HEA). The small area of rupture propagation (Figure B4) and the relatively small amount of slip results in relatively small vertical seafloor displacements of up to ∼0.56 m, southeast of Crete. The moment magnitude of $M_W \sim 7.5$ is the smallest among all models.

4.6. Shake Maps

We compare shake maps, spatial distributions of the modeled rotationally independent geometric mean at 50% of the horizontal peak ground velocities (PGVs), for three margin-wide dynamic rupture models (HE, HW, HEP) and three non-margin-wide rupture models (HEA, DCA, DCAS). By this means, we investigate—to first order—how epicentral location, rupture directivity, off-fault plasticity, and increasing initial condition complexity influence long-period peak ground motions (Figure 10). We note that our models have a relatively high resolution of up to 2.7 Hz of the seismic wavefield close to the slab but have gradually decreasing resolution away from it (Section 2.1). This allows us to explore several dynamic rupture scenarios efficiently. However, dynamic rupture simulations with constant high resolution in a larger region would be required for physics-based ground motion simulations in the frequency band of interest to earthquake engineering (Taufiqurrahman et al., 2022; Uphoff et al., 2017).

We find that the modeled amplitude of PGVs may double between different epicentral locations. Off-fault plastic yielding limits the overall amplitudes of PGVs and the spatial extent of high shaking. The smallest moment magnitude scenario (DCAS) does not produce the smallest PGVs. The high stress drop model DCA is producing relatively high PGVs.

In model HE (eastern hypocenter location), the distribution of high PGV reflects the location and shape of the highest fault slip, located south-west of Crete and Peloponnese, where PGVs reach ~0.6 m/s (Figure 10a). Peloponnese, Crete, and the Southern Aegean Sea islands are affected by PGVs of ~0.3–0.4 m/s. PGV decreases with distance from the trench. We observe relatively higher ground motion in the direction of rupture propagation on the fault toward Sicily and in the South toward the coast of Libya.

For model HEP, the PGV distribution is similar, with the highest PGVs toward the west, in the rupture directivity direction (Figure 10d). Nevertheless, the area of high PGVs is narrower than for model HE. In addition, the effect of directivity, leading to high PGVs toward Sicily, is less than for model HE. HEP generates ~0.1 m/s smaller peak ground velocity at the Libyan coast (~0.1–0.2 m/s). The smaller area of high PGVs can be explained by the energy loss within the off-fault plastic material (Andrews, 2005; Dunham et al., 2011; Gabriel et al., 2013), contributing to the fracture energy. Roten et al. (2018) show that materials of low strength, such as unconsolidated sediments, can reduce PGVs by 15%–30% in a continental strike-slip setting. Our results for the HASZ with a local PGV reduction of ~30%–50% agree with these estimates.

For model HW (western hypocenter location), the directivity of rupture propagation leads to a different PGV distribution than model HE. The highest PGVs of ~1.0 m/s are located further southwest above the shallow Hellenic Arc (Figure 10b). The high slip rate on the shallow fault (Section 3.1 and Figure 4) produces PGVs up to ~0.5 m/s higher than the maximum PGVs in model HE. The Peloponnese is barely affected by ground motions, while we note high PGVs south of Crete that affect the Lybian and Egyptian coasts ranging from ~0.4–0.9 m/s.

For model DCA, the highest PGVs of ~1.0 m/s are located northeast of Crete (Figure 10e). In this scenario, only the eastern coastal part of Crete Island experiences high PGV. High PGVs are directed toward the northeast due to directivity effects. For this model, the smaller islands northeast of Crete are mostly affected by high PGVs of ~0.5–0.6 m/s. We observe PGVs of ~0.4 m/s at Rhodes and PGVs of ~0.2 m/s affecting the Turkish coast. The maximum PGV amplitudes of ~1.0 m/s in model DCA are larger than for model HE and HEP, likely reflecting the higher stress drop and higher slip rates, and ultimately the locally shorter critical slip weakening distances (Figure 6).

In model DCAS, the highest PGVs of ~0.06–0.2 m/s appear concentrated to southeast Crete (Figure 10c). Directivity effects imprint on PGV distributions. Compared to model DCA, the maximum PGVs are relatively small (~0.45 m/s smaller), which is in agreement with the model's smaller stress drop (Figure 6) and its ~93% lower peak slip rate amplitudes (Table 2).

The single asperity model HEA shows the smallest PGVs among the models located southeast of Crete with a maximum amplitude of ~0.02 m/s. While the moment magnitude of this event is similar to that of model DCA (Table 2), the peak amplitude of peak slip rate and stress drop of model HEA are ~93% and ~50% smaller than for model DCA (Figures 8b, 6f, B1a and B2a).

5. Discussion

5.1. The AD 365 Earthquake and Tsunami

Large ground deformation during the AD 365 event is assumed to have caused large tsunami amplitudes (e.g., Stiros & Drakos, 2006). We show that earthquakes similar in magnitude to the historical AD 365 earthquake might not solely be mechanically plausible on splay faults branching the main megathrust but on the Hellenic Arc subduction interface itself. In model HEP, we allow weak off-slab sediments to plastically deform during earthquake rupture. We show that sediments may play an important role in causing locally high seafloor uplift. The high amount of off-fault plastic deformation (Figure 7) generates a higher vertical displacement (Figure 4d) compared to the purely elastic model, while rupture propagation in the slip-strengthening region remains limited (Figures 4d and

6). In addition, including multi-scale D_c-asperities in our model significantly enhances the seafloor uplift. All these effects together may help to explain what caused historical tsunamis, such as the AD 365 earthquake.

The amount of vertical uplift (∼3 m) in the model with off-fault plasticity (HEP) is twice as large as the uplift modeled when considering a purely elastic rheology (HE model). However, it is still not comparable to the coseismic uplift of ∼10 m inferred for the AD 365 earthquake from seamarks, fallen blocks, co-seismic seafloor uplift, and tsunami modeling around western Crete (Spratt, 1865; Flemming, 1978; Pirazzoli et al., 1982; Stiros & Drakos, 2006; Shaw et al., 2008; England et al., 2015), associated with large (∼7 m) tsunami layer deposits (Pirazzoli et al., 1992).

The HEP model generates a maximum accumulated on-fault slip of ∼22 m, which is significantly higher than the slip of all other models: Compared to model HE (1.6 m uplift), the twice larger fault slip leads to twice as high peak vertical seafloor displacements (2.9 m) off-shore of southwestern Crete. The peak accumulated fault slip in model HEP is comparable to the maximum amount of slip from Papadimitriou and Karakostas (2008), although the moment magnitude of our model is higher ($M_W \sim 9$ compared to $M_W 8.4$), which may be due to our simplified subsurface velocity model.

The on-fault D_c heterogeneities in the DCA model lead to high accumulated on-fault slip, which is ∼1.5 m higher in amplitude than in the margin-wide $M_W 9$ rupture model HE. Wirp et al. (2021) show that an increase in D_c (i.e., increased fracture energy (Cocco et al., 2023; Kammer et al., 2024; Rice, 1980),) can enhance megathrust on-fault slip significantly and lead to larger tsunamis. The DCA model produces a moment magnitude of $M_W \sim 8.4$, demonstrating that the multi-scale asperity approach, incorporating the expected but hard-to-constrain heterogeneities in subduction zones, offers an efficient way to parameterize earthquake rupture extents on an otherwise smooth and non-segmented subduction interface geometry. The DCA model generates a peak vertical seafloor displacement of ∼3.5 m, which is much larger than in the other $M_W \sim 8$ models we propose. While the specific characteristics of the DCA rupture model originate from the assumed multi-scale D_c variations, we expect that alternative models with (scale-dependent) heterogeneous fault stress, for example, constrained by past seismicity, could achieve similar characteristics, such as a limited rupture extent and a more complex rupture process (e.g., Oral et al., 2022).

Combining the segmented stress and the multi-scale asperity models further reduces the modeled moment magnitude to $M_W 7.5$, rendering model DCAS as our scenario with the smallest M_W. The combination of regions of unfavorably oriented stress and on-fault heterogeneities effectively limit moment magnitude in our dynamic rupture scenarios.

5.2. Modeling the 1303 Earthquake as Constrained by a Single Asperity Versus Stress Segmentation

In the following, we compare two different approaches to modeling dynamic rupture earthquake scenarios yielding magnitudes similar to the 1303 Crete earthquake ($M_W \sim 8$) on the Hellenic Arc megathrust itself. Both dynamic rupture examples have hypocenter locations and seafloor uplift that may resemble the 1303 earthquake. First, we discuss that prescribing a single fault stress asperity (model HEA) is an efficient way to limit earthquake dynamic rupture slip and moment magnitude. Second, regionally segmented initial stress based on stress inversions (model HES) also acts as an efficient barrier.

5.2.1. The Single Asperity Approach

The moment magnitude of the single asperity model (HEA, $M_W 8.04$) fits the moment magnitude inferred for the 1303 earthquake (Papazachos et al., 1999). However, the modeled maximum vertical seafloor uplift of ∼1.29 m is relatively low compared to Necmioğlu and Özel (2014), who use a displacement of 9 m as a source for their tsunami model representing the 1303 event. The vertical seafloor uplift in our model can be explained by the relatively deep location of the hypocenter and the slipping asperity, in conjunction with the low on-fault slip modeled. We conclude that a fault stress asperity offers a simple way to effectively restrict rupture propagation to a predefined fault area.

5.2.2. The Segmented Stress Model

Accounting for along-arc variations of regional stress orientation as constrained by stress inversions allows modeling non-margin-wide ruptures. In several regions, the constrained regional stress does not promote rupture propagation across the megathrust, which can lead to spontaneous rupture arrest. The partial ruptures using the segmented stress model are associated with 6.1% (HMS) and 53.7% (HES) lower on-fault slip than the margin-wide rupture scenarios. With moment magnitudes of $M_W = 8.81$ (HMS) and $M_W = 8.12$ (HES) and maximum seafloor uplifts of 1.71 m (HMS) and 1.17 m (HES), the two segmented stress models are comparable to maximum events proposed for tsunami studies in the Hellenic arc area (e.g., S. Tinti et al., 2005; Yolsal et al., 2007; Lorito et al., 2008; Necmioğlu & Özel, 2014).

The moment magnitude, hypocenter location, and distribution of the seafloor deformation of the HES model resemble scenarios of the 1303 Crete earthquake modeled by Necmioğlu and Özel (2014). We, nevertheless, note that the fault slip and associated ground deformation pattern of this event are poorly constrained. As an illustration, Yolsal et al. (2007) model the 1303 Crete earthquake and the associated tsunami using a smaller southeast striking, northeast dipping fault plane. Due to the fault orientation, their assumed initial water displacement caused by the 1303 event is different than what we would expect from the seafloor displacement of the HES model. Their modeled northwest-southeast oriented uplift of the water column, located south of Crete, disagrees with the rupture propagation direction in our models that causes southwest-northeast oriented seafloor uplift.

5.3. Shake Maps

We find that maximum PGVs vary by epicentral locations among the models, but highly depend on shallow slip into the slip-strengthening region of the fault. Thus, models with a western hypocenter lead to a broader extent of higher PGVs, compared to a hypocenter on the eastern Hellenic Arc. High stress drop of model DCA produces relatively high PGVs, which are localized northeast of Crete island. The models DCA, DCAS, and HEA, which are all M ∼ 8–8.5 magnitude events, are not able to reproduce a shaking that we believe would be great enough to cause tsunamis compared to the AD365 or 1303 Crete events. Allowing for off-fault plastic yielding doubles the amount of on-fault slip and nearly doubles the maximum vertical seafloor displacement directly above the fault interface while simultaneously limiting the spatial distribution of high PGVs. These compound effects, characterized by increased on-fault slip and larger but more localized uplift in model HEP, align with previous dynamic rupture models in various tectonic contexts (Kaneko & Fialko, 2011; Ma, 2008b, 2022; Ma & Andrews, 2010; Roten et al., 2014, 2017; Ulrich et al., 2022). Off-fault plastic yielding leads to a redistribution of stress and energy that allow for more sustained slip over a larger area, while at the rupture front, the peak slip rate remains limited.

5.4. Implications for Regional Earthquake and Tsunami Hazard Assessments

Probabilistic seismic hazard analysis (PSHA), seismic-probabilistic tsunami hazard assessment (S-PTHA) models, as well as tsunami early warning systems, often utilize uniform or stochastic source models; however, these may not fully represent dynamic rupture and tsunami generation complexity. Our study illustrates the key driving factors and ingredients for realistic 3D dynamic rupture models for earthquake scenarios in the Hellenic Arc region. For example, we show that earthquakes comparable in moment magnitude and slip to the AD 365 and 1303 Crete earthquakes can be dynamically viable on the megathrust itself. This finding may support the assumptions underlying the NEAMTHM18 model (Basili et al., 2021), which is the reference regional hazard model for the Tsunami Early Warning and Mitigation System in the North-eastern Atlantic, the Mediterranean and connected sea (NEAMTWS).

For different source locations among our models, the evolving on-fault rupture dynamics and thus, fault slip, peak slip rates, stress drop, and seafloor displacement are highly variable. Specifically, the presented scenarios differ in shallow slip and potentially lead to complex near trench seafloor uplift, which in turn affects PGV distribution (Figures 4 and 10).

Tsunami models based on kinematic or statically derived slip distributions may account for shallow slip amplification (Scala et al., 2020). However, kinematic models are highly non-unique (Mai et al., 2016; Wong et al., 2023) and may lack the physical self-consistency of dynamic models that can jointly describe spontaneously evolving on-fault slip distribution, seafloor uplift, and peak ground velocities capturing their interplay.

Addressing epistemic uncertainty remains challenging (e.g., Atkinson et al., 2014; Bommer & Scherbaum, 2008; Gómez Zapata et al., 2022; Rodriguez-Marek et al., 2021; Tarbali et al., 2018). Various modeling approaches, such as static, kinematic, and dynamic earthquake models, could be used jointly and differently weighted (Marzocchi et al., 2015). For example, physics-based dynamic rupture models may form differently weighted alternatives within an established PTHA logic tree used in ensemble modeling (L. Li et al., 2016). The CyberShake model is a prominent example that incorporates physics-based 3D ground motion simulations and wave propagation effects in their seismic hazard calculations for southern California (Maechling et al., 2007; Graves et al., 2011; X. Meng et al., 2023; Moschetti et al., 2023).

Dynamic rupture models may also be used to directly explore natural earthquake variability (Gallovič & Valentova, 2020; Ripperger et al., 2008; Schmedes et al., 2010) - often treated as aleatory in S-PTHA (e.g., Gibbons et al., 2020; Lorito et al., 2014; Selva et al., 2016; Souty & Gailler, 2021). This would require computational optimization and resources to allow for running sufficiently many scenarios (e.g., Panzera et al., 2016; B. Li et al., 2023; Folch et al., 2023). To keep computational costs low, dynamic rupture models may help to constrain and to inform less computationally expensive stochastic scenarios (e.g., Murphy et al., 2016; Savran & Olsen, 2020).

5.5. Limitations of This Work

We here do not show models of smaller earthquakes ($M_W < 7.5$), which likely requires including smaller-scale heterogeneity, that is, smaller size asperities (Blaser et al., 2010; Murotani et al., 2008; Strasser et al., 2010) or fault roughness (Candela et al., 2011; Griffith et al., 2010; Zielke et al., 2017). Instead, we model counterfactual along-arc rupture propagation scenarios (HE, HM, HW, HER) and reproduce magnitudes (HEA, HES) and potential displacements (HEP, DCA) of historic events. Our 3D simulations are computationally challenging, as we include a large part of the megathrust interface, across which the rupture process zone and asperities need to be resolved, and a large portion of the east Mediterranean region to make our simulations applicable to source tsunami simulations.

Smaller magnitude earthquakes ($M_W < 7$) with high tsunamigenic potential (Bocchini et al., 2020) may occur on splay faults, which we do not consider in this study (Ganas et al., 2020; Kiratzi, 2013; Papadimitriou et al., 2016; Wendt et al., 2009). Specifically, high-angle reverse faults in the upper plate above the plate interface may add to the tsunamigenic potential of inter-plate earthquakes (DeDontney & Rice, 2012; Fukao, 1979; Lotto et al., 2019; van Zelst et al., 2022) and should be explored in future studies.

Our ground motion and shake map analysis is meaningful in a relative sense - to compare between scenarios - but is limited by the simplified 1D velocity model we use and by the resolution of 1.75 Hz. For example, Causse et al. (2023) illustrate, based on rupture propagation models, that local basin amplification effects (in thick sediments) can dominate regional ground motion accelerations in the Mediterranean.

6. Conclusions

We demonstrate mechanically self-consistent approaches to constrain realistic and heterogeneous initial conditions integrating available observations for Hellenic Arc subduction zone (HASZ) 3D dynamic rupture earthquake scenarios. We analyze an ensemble of 10 3D dynamic rupture earthquake scenarios utilizing a realistic slab geometry in combination with increasing levels of initial condition complexity, from homogeneous to heterogeneous initial stress conditions, and from single-asperity to stochastic multi-scale asperity models.

Our ensemble of 10 dynamic rupture simulations illustrates various aspects of the dynamic variability of fault slip and uplift. Models with different epicentral locations and homogeneous initial conditions represent counterfactual margin-wide scenarios reaching $M_W \sim 9$. Dynamic rupture propagates into shallow slip-strengthening portions of the slab. The further west the epicenter location, the more shallow slip is dynamically generated and, consequently, the more pronounced the modeled localized near-trench uplift becomes. A slightly more shallowly plunging maximum compressive stress leads to spontaneous rupture arrest before crossing the complete margin, generating a moment magnitude of $M_W 8.61$ but a similar maximum vertical displacement of ~ 1.6 m compared to the margin-wide rupture scenarios. Off-fault plastic deformation of unconsolidated sediments efficiently prevents shallow fault slip, reduces local PGVs by about ~30%–50%, and doubles the amount of seafloor uplift. A prescribed prestress asperity dynamic rupture earthquake scenario effectively limits fault slip to a moment magnitude similar to the 1303 Crete event. Incorporating regional along-strike variations of the initial stress, constrained by stress inversion, limits dynamic rupture propagation and slip to the deeper slip-weakening region of the slab. The resulting $M_W \sim 8.5$ earthquakes show complex uplift patterns reflecting the more heterogeneous initial conditions. Adding multi-scale, randomly distributed frictional asperities leads to five times higher peak slip rates than in the other models and causes the largest seafloor displacements of up to ~3.5 m. In the most complex model, we combine a multi-scale asperity approach with the regional along-arc segmented prestress, resulting in the highly heterogeneous rupture propagation and the smallest rupture area.

This study is a first step toward including dynamic rupture modeling in regional Hellenic Arc seismic and seismic-tsunami hazard assessment. Our approach of constraining dynamic rupture initial conditions with increasing levels of complexity can be valuable for other, mostly 'quiet' subduction zones, such as the Cascadia subduction zone, as it may provide a catalog of physics-based scenarios suitable to inform hazard assessment and disaster risk management planning in the absence of long and complete historical records.

Appendix A: Computational Mesh Used for All Ten Dynamic Rupture Simulations

We show the computational mesh to illustrate the mesh resolution and coarsening away from the fault.

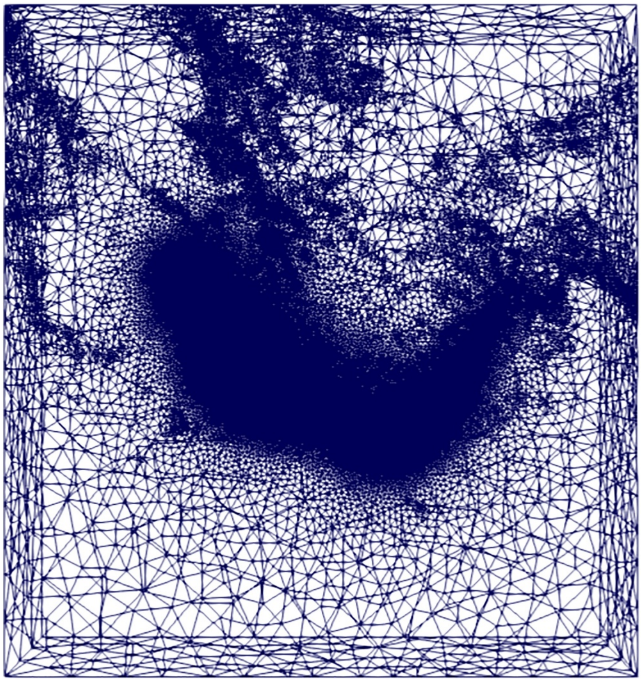

Figure A1. Top view on the wireframe of the computational mesh used to run the DR models of this study. Note the fine mesh resolution above the fault and the mesh coarsening to the simulation boundaries.

Appendix B: Close-Up Views of Dynamic Rupture Simulation Results

We show close-up views of chosen results of dynamic rupture simulations to better visualize small-scale rupture characteristics compared to the spatial extent of the slab. Due to the smaller rupture in models HEA, HES, and DCAS, it is helpful to zoom in on the fault area where rupture propagation occurs and the surface area where we observe uplift. For models HER, HEA, HMS, HES, DCA, and DCAS, we add a closeup after 20 s rupture propagation to better visualize differences in dynamics at this early stage of rupture propagation. All figures relate to figures in the results section (Section 4).

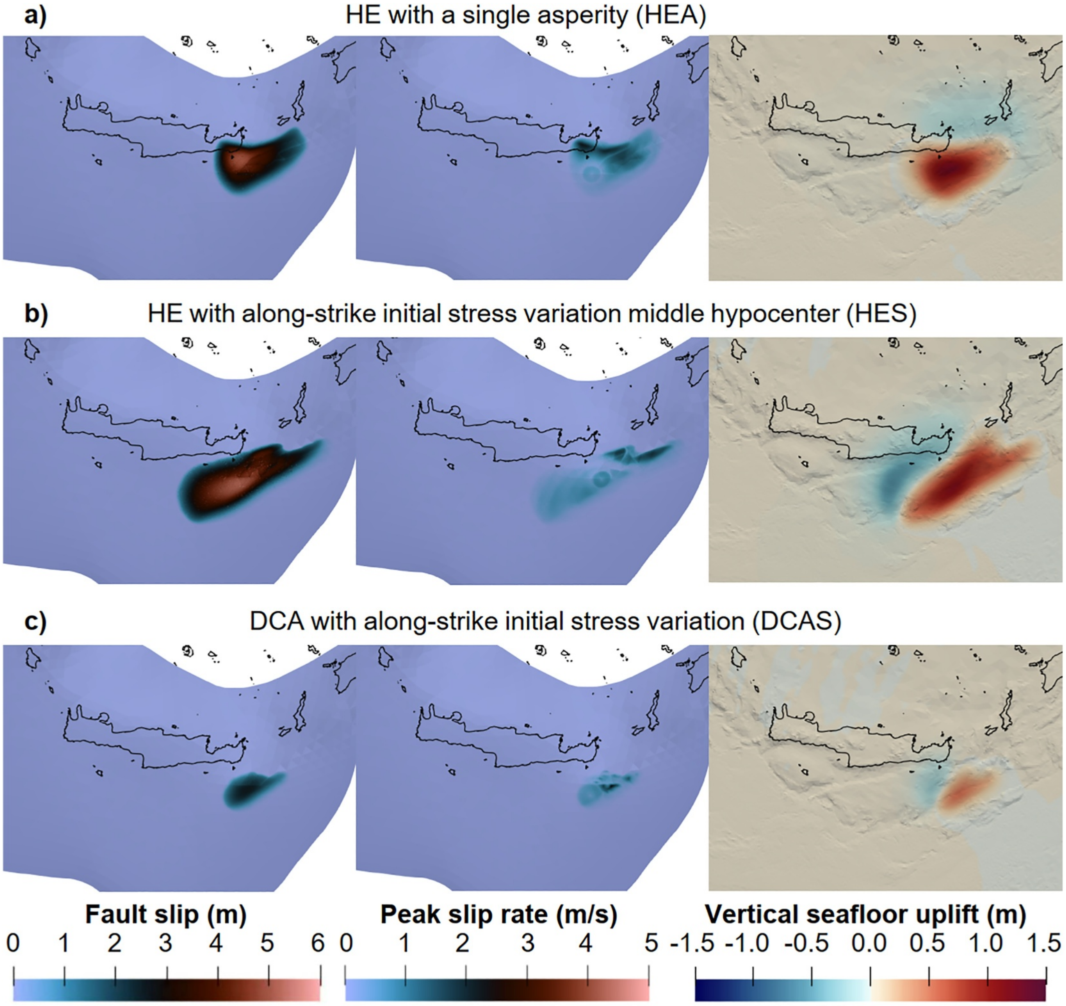

Figure B1. Close-up of rupture characteristics of model HEA, HES and DCAS: Zoom in of Figures 8b–8d, and e showing the final fault slip, peak slip rate, and vertical seafloor displacement. The color scales are saturated. For absolute maximum values see Table 2. Areas of high PSR do not coincide with areas of high fault slip. The vertical seafloor displacement mirrors the final on-fault slip. The seafloor subsidence for HES is more pronounced than for HEA and DCAS.

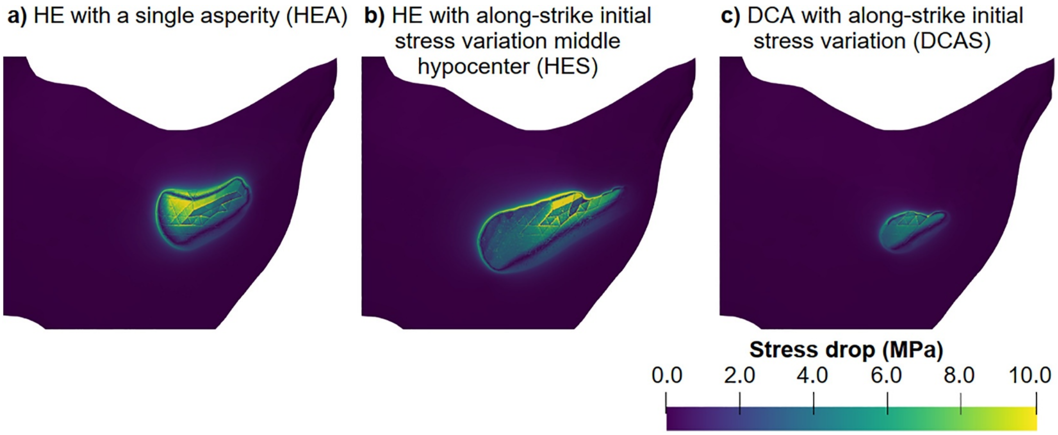

Figure B2. Stress drop for model HEA, HES, and DCAS: Close-up of Figures 6f–6 h and 6j. For HES, the stress drop is highest at the steeper dipping fault, whereas the stress drop of HEA and DCAS is homogeneously distributed.

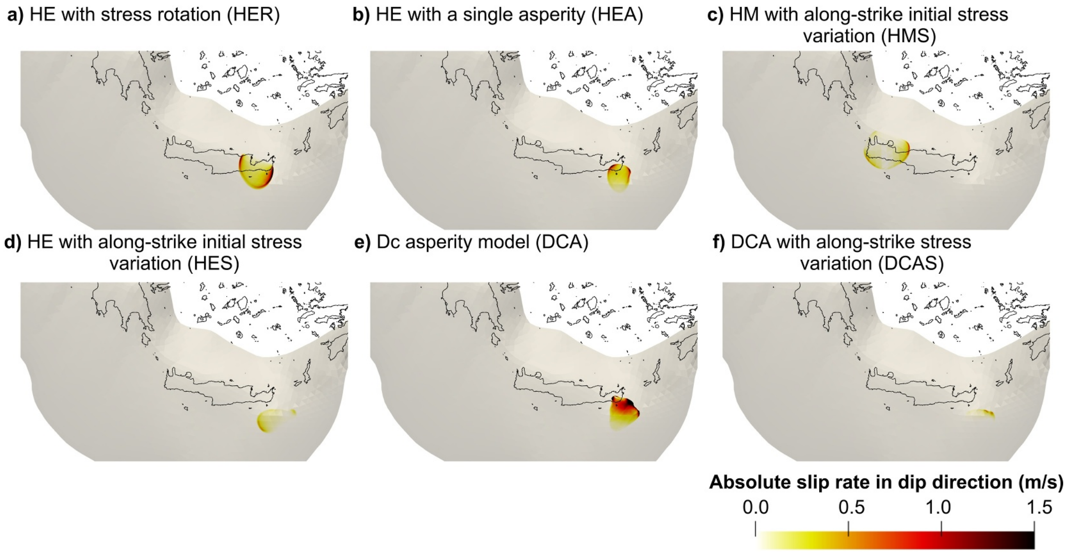

Figure B3. Close-up of Figure 9: Slip rate in dip direction for simulations HER (a), HEA (b), HMS (c), HES (d), DCA (e), and DCAS (f) at 20 s simulation time. Note the bilateral rupture evolution for models HER, HEA, and HMS. For DCA, the slip rate is highest, whereas the smaller moment magnitude DCAS scenario experiences a lower slip rate than all other models.

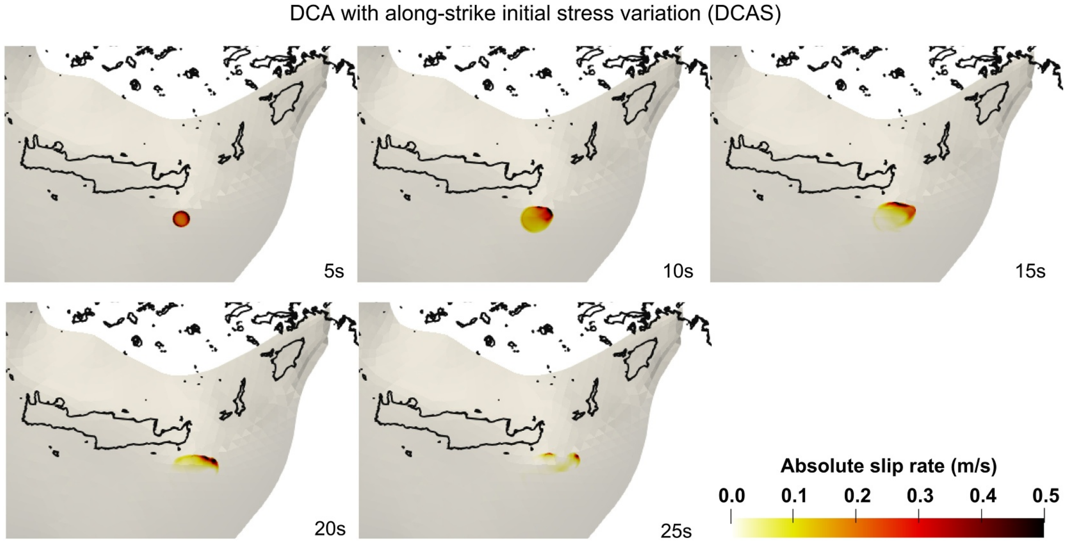

Figure B4. Close-up of Figure 9f: Slip rate in dip direction for simulation DCAS at 5, 10, 15, 20, and 25 s simulation time. Note the changed color scale compared to Figures 9 and B3.

Conflict of Interest

The authors declare no conflicts of interest relevant to this study.

Data Availability Statement

We use the open-software package SeisSol (www.seissol.org), available at https://github.com/SeisSol/SeisSol, commit #gdf6b18ee, master branch (Uphoff et al. (2022)) to perform all dynamic rupture simulations presented in this study. All simulation input files can be downloaded from Wirp et al. (2024). Instructions for downloading, installing and running the code are described in the SeisSol documentation (https://seissol.readthedocs.io/en/

latest/). Instructions for setting up and running simulations are at https://seissol.readthedocs.io/en/latest/configuration.html. Quickstart containerized installations and introductory materials are provided in the docker container and Jupyter Notebooks at https://github.com/SeisSol/Training. Example problems and model configuration files are provided at https://github.com/SeisSol/Examples, many of which reproduce the SCEC 3D dynamic rupture benchmark problems described at https://strike.scec.org/cvws/benchmark_describtions.html.

Acknowledgments

We thank the Editor Satoshi Ide, the Associate Editor, and two anonymous reviewers for their thoughtful and constructive comments. We thank Janina Moser for her initial analysis as part of her Bachelor's thesis. We thank Lukas Krenz and Michael Bader for their technical expertise. This work was supported by the European Union's Horizon 2020 Research and Innovation Program (TEAR ERC Starting grant agreement No. 852992), Horizon Europe (ChEESE-2P Grant 101093038, DT-GEO Grant 101058129 and Geo-INQUIRE Grant 101058518), the National Science Foundation (Grant EAR-2225286, EAR-2121568, OAC-2139536, OAC-2311208), and the National Aeronautics and Space Administration (80NSSC20K0495). The authors acknowledge the Gauss Centre for Supercomputing e.V. (www.gauss-centre.eu, projects pr63qo, pn68fi, pr83no, pn49ha) for funding this project by providing computing time on the GCS Supercomputer SuperMUC-NG at Leibniz Supercomputing Centre (www.lrz.de). Computing resources were also provided by the Institute of Geophysics of LMU Munich Oeser et al. (2006). Open Access funding enabled and organized by Projekt DEAL.

References

Abrahams, L. S., Krenz, L., Dunham, E. M., Gabriel, A.-A., & Saito, T. (2023). Comparison of methods for coupled earthquake and tsunami modelling. *Geophysical Journal International*, *234*(1), 404–426. https://doi.org/10.1093/GJI/GGAD053

Altinok, Y., & Ersoy, S. (2000). Tsunamis observed on and near the Turkish coast. *Natural Hazards*, *21*, (2/3), 185–205. https://doi.org/10.1007/978-94-017-2386-2_5

Ambraseys, N. (2009). *Earthquakes in the mediterranean and Middle East: A multidisciplinary study of seismicity up to 1900* (Vol. 136). Cambridge University Press. https://doi.org/10.1017/CBO9781139195430.004

Ambraseys, N. N. (1962). Data for the investigation of the seismic sea-waves in the Eastern Mediterranean. *Bulletin of the Seismological Society of America*, *52*, 895–913. https://doi.org/10.1785/BSSA0520040895

Ambraseys, N. N. (1994). Material for the investigation of the seismicity of Libya. *Libyan Studies*, *25*, 7–22. https://doi.org/10.1017/S0263718900006191

Amlani, F., Bhat, H. S., Simons, W. J., Schubnel, A., Vigny, C., Rosakis, A. J., et al. (2022). Supershear shock front contribution to the tsunami from the 2018 {\text{M}}_{W} 7.5 Palu, Indonesia earthquake. *Geophysical Journal International*, *230*(3), 2089–2097. https://doi.org/10.1093/GJI/GGAC162

Andrews, D. J. (2005). Rupture dynamics with energy loss outside the slip zone. *Journal of Geophysical Research*, *110*(B1). https://doi.org/10.1029/2004JB003191

Angelier, J. (1990). Inversion of field data in fault tectonics to obtain the regional stress—III. A new rapid direct inversion method by analytical means. *Geophysical Journal International*, *103*(2), 363–376. https://doi.org/10.1111/j.1365-246X.1990.tb01777.x

Antonopoulos, J. (1980). Data from investigation on seismic sea-waves events in the Eastern Mediterranean from the birth of Christ to 500 AD. *Annals of Geophysics*, *33*, 141–161.

Aochi, H., & Madariaga, R. (2003). The 1999 Izmit, Turkey, earthquake: Nonplanar fault structure, dynamic rupture process, and strong ground motion. *Bulletin of the Seismological Society of America*, *93*(3), 1249–1266. https://doi.org/10.1785/0120020167

Atkinson, G. M., Bommer, J. J., & Abrahamson, N. A. (2014). Alternative approaches to modeling epistemic uncertainty in ground motions in probabilistic seismic-hazard analysis. *Seismological Society of America*, *85*(6), 1141–1144. https://doi.org/10.1785/0220140120

Bartolomeo, M. D., Meziane, A., Massi, F., Baillet, L., & Fregolent, A. (2010). Dynamic rupture at a frictional interface between dissimilar materials with asperities. *Tribology International*, *43*(9), 1620–1630. https://doi.org/10.1016/j.triboint.2010.03.008

Basili, R., Brizuela, B., Herrero, A., Iqbal, S., Lorito, S., Maesano, F. E., et al. (2021). The making of the NEAM tsunami hazard model 2018 (NEAMTHM18). *Frontiers in Earth Science*, *8*. https://doi.org/10.3389/FEART.2020.616594

Basili, R., Tiberti, M. M., Kastelic, V., Romano, F., Piatanesi, A., Selva, J., & Lorito, S. (2013). Integrating geologic fault data into tsunami hazard studies. *Natural Hazards and Earth System Sciences*, *13*(4), 1025–1050. https://doi.org/10.5194/nhess-13-1025-2013

Bassett, D., & Watts, A. B. (2015). Gravity anomalies, crustal structure, and seismicity at subduction zones: 1. Seafloor roughness and subducting relief. *Geochemistry, Geophysics, Geosystems*, *16*(5), 1508–1540. https://doi.org/10.1002/2014GC005684

Becker, D., & Meier, T. (2010). Seismic slip deficit in the southwestern Forearc of the Hellenic subduction zone. *Bulletin of the Seismological Society of America*, *100*(1), 325–342. https://doi.org/10.1785/0120090156

Behrens, J., Løvholt, F., Jalayer, F., Lorito, S., Salgado-Gálvez, M. A., Sørensen, M., et al. (2021). Probabilistic tsunami hazard and risk analysis: A review of research gaps. *Frontiers in Earth Science*, *9*. https://doi.org/10.3389/feart.2021.628772

Biemiller, J., Gabriel, A.-A., & Ulrich, T. (2023). Dueling dynamics of low-angle normal fault rupture with splay faulting and off-fault damage. *Nature Communications*, *14*(1), 2352. https://doi.org/10.1038/s41467-023-37063-1

Bird, P. (2003). An updated digital model of plate boundaries. *Geochemistry, Geophysics, Geosystems*, *4*(3). https://doi.org/10.1029/2001GC000252

Blaser, L., Krüger, F., Ohrnberger, M., & Scherbaum, F. (2010). Scaling relations of earthquake source parameter estimates with special focus on subduction environment. *Bulletin of the Seismological Society of America*, *100*(6), 2914–2926. https://doi.org/10.1785/0120100111

Bocchini, G. M., Novikova, T., Papadopoulos, G., Agalos, A., Mouzakiotis, E., Karastathis, V., & Voulgaris, N. (2020). Tsunami potential of moderate earthquakes: The July 1, 2009 earthquake (M_{W} 6.45) and its associated local tsunami in the Hellenic Arc. *Pure and Applied Geophysics*, *177*(3), 1315–1333. https://doi.org/10.1007/s00024-019-02246-9

Bohnhoff, M., Harjes, H. P., & Meier, T. (2005). Deformation and stress regimes in the Hellenic subduction zone from focal Mechanisms. *Journal of Seismology*, *9*(3), 341–366. https://doi.org/10.1007/S10950-005-8720-5

Bohnhoff, M., Makris, J., Papanikolaou, D., & Stavrakakis, G. (2001). Crustal investigation of the Hellenic subduction zone using wide aperture seismic data. *Tectonophysics*, *343*(3–4), 239–262. https://doi.org/10.1016/S0040-1951(01)00264-5

Bommer, J. J., & Scherbaum, F. (2008). The use and misuse of logic trees in probabilistic seismic hazard analysis. *Earthquake Spectra*, *24*(4), 997–1009. https://doi.org/10.1193/1.2977755

Bormann, P. (2009). Global 1-D Earth models. In *New manual of seismological observatory practice (nmsop)* (pp. 1–12). Deutsches GeoForschungsZentrum GFZ.

Bourgois, J., Martin, H., Lagabrielle, Y., Le Moigne, J., & Frutos Jara, J. (1996). Subduction erosion related to spreading-ridge subduction: Taitao peninsula (Chile margin triple junction area). *Geology*, *24*(8), 723–726. https://doi.org/10.1130/0091-7613(1996)024⟨0723:SERTSR⟩2.3.CO;2

Byerlee, J., & Summers, R. (1976). A note on the effect of fault gouge thickness on fault stability. *International Journal of Rock Mechanics and Mining Sciences and Geomechanics Abstracts*, *13*(1), 35–36. https://doi.org/10.1016/0148-9062(76)90226-6

Candela, T., Renard, F., Schmittbuhl, J., Bouchon, M., & Brodsky, E. E. (2011). Fault slip distribution and fault roughness. *Geophysical Journal International*, *187*(2), 959–968. https://doi.org/10.1111/j.1365-246X.2011.05189.x

Casten, U., & Snopek, K. (2006). Gravity modelling of the Hellenic subduction zone—A regional study. *Tectonophysics*, *417*(3), 183–200. https://doi.org/10.1016/j.tecto.2005.11.002

Causse, M., Maufroy, E., André, L., & Bard, P. (2023). What was the level of ground motion across Europe during the great A.D. 365 Crete earthquake? *Seismological Research Letters*, *94*(5), 2397–2410. https://doi.org/10.1785/0220220385

Chan, Y. P. B., Yao, S., & Yang, H. (2023). Impact of hypocenter location on rupture extent and ground motion: A case study of southern cascadia. *Journal of Geophysical Research: Solid Earth*, *128*(8), e2023JB026371. https://doi.org/10.1029/2023JB026371

Chousianitis, K., & Konca, A. O. (2021). Rupture process of the 2020 {\text{M}}_{W}7.0 Samos earthquake and its effect on surrounding active faults. *Geophysical Research Letters*, *48*(14), e2021GL094162. https://doi.org/10.1029/2021GL094162

Cocco, M., Aretusini, S., Cornelio, C., Nielsen, S. B., Spagnuolo, E., Tinti, E., & Di Toro, G. (2023). Fracture energy and breakdown work during earthquakes. *Annual Review of Earth and Planetary Sciences*, *51*(1), 217–252. https://doi.org/10.1146/annurev-earth-071822-100304

Cocco, M., Tinti, E., & Cirella, A. (2016). On the scale dependence of earthquake stress drop. *Journal of Seismology*, *20*(4), 1151–1170. https://doi.org/10.1007/s10950-016-9594-4

Dalguer, L. A., Miyake, H., Day, S. M., & Kikura, K. (2008). Surface rupturing and buried dynamic-rupture models calibrated with statistical observations of past earthquakes. *Bulletin of the Seismological Society of America*, *98*(3), 1147–1161. https://doi.org/10.1785/0120070134

Das, S., & Aki, K. (1977). Fault plane with barriers: A versatile earthquake model. *Journal of Geophysical Research*, *82*(36), 5658–5670. https://doi.org/10.1029/JB082i036p05658

Davies, G., Griffin, J., Løvholt, F., Glimsdal, S., Harbitz, C., Thio, H. K., et al. (2018). A global probabilistic tsunami hazard assessment from earthquake sources. *Geological Society - Special Publications*, *456*(1), 219–244. https://doi.org/10.1144/SP456.5

DeDontney, N., & Rice, J. R. (2012). Tsunami wave analysis and possibility of splay fault rupture during the 2004 Indian Ocean earthquake. *Pure and Applied Geophysics*, *169*(10), 1707–1735. https://doi.org/10.1007/s00024-011-0438-40

de la Puente, J., Ampuero, J.-P., & Käser, M. (2009). Dynamic rupture modeling on unstructured meshes using a discontinuous galerkin method. *Journal of Geophysical Research*, *114*(B10). https://doi.org/10.1029/2008JB006271

DeMets, C., Gordon, R. G., Argus, D., & Stein, S. (1990). Current plate motions. *Geophysical Journal International*, *101*(2), 425–478. https://doi.org/10.1111/j.1365-246X.1990.tb06579.x

DeMets, C., Gordon, R. G., Argus, D. F., & Stein, S. (1994). Effect of recent revisions to the geomagnetic reversal time scale on estimates of current plate motions. *Geophysical Research Letters*, *21*(20), 2191–2194. https://doi.org/10.1029/94GL02118

DiVita, A. (1979). *I terremoti a Gortina in età romana e proto-bizantina* (pp. 61–62). ASA.

DiVita, A. (1995). Archaeologists and earthquakes, the case of 365 A.D. *Annals of Geophysics*, *38*(5–6), 971–976. https://doi.org/10.4401/ag-4097

Du, Y., Ma, S., Kubota, T., & Saito, T. (2021). Impulsive tsunami and large runup along the Sanriku coast of Japan produced by an inelastic wedge deformation model. *Journal of Geophysical Research: Solid Earth*, *126*(8), e2021JB022098. https://doi.org/10.1029/2021JB022098

Dumbser, M., & Käser, M. (2006). An arbitrary high-order discontinuous galerkin method for elastic waves on unstructured meshes — II. The three-dimensional isotropic case. *Geophysical Journal International*, *167*(1), 319–336. https://doi.org/10.1111/j.1365-246X.2006.03120.x

Dunham, E. M., Belanger, D., Cong, L., & Kozdon, J. E. (2011). Earthquake ruptures with strongly rate-weakening friction and off-fault plasticity, Part 1: Planar faults. *Bulletin of the Seismological Society of America*, *101*(5), 2296–2307. https://doi.org/10.1785/0120100075

Dziewonski, A. M., & Anderson, D. L. (1981). Preliminary reference Earth model. *Physics of the Earth and Planetary Interiors*, *25*(4), 297–356. https://doi.org/10.1016/0031-9201(81)90046-7

Elliott, J., & Freymueller, J. T. (2020). A block model of present-day kinematics of Alaska and western Canada. *Journal of Geophysical Research: Solid Earth*, *125*(7), e2019JB018378. https://doi.org/10.1029/2019JB018378

England, P., Howell, A., Jackson, J., & Synolakis, C. (2015). Palaeotsunamis and tsunami hazards in the eastern mediterranean. *Philosophical Transactions of the Royal Society A: Mathematical, Physical & Engineering Sciences*, *373*(2053), 20140374. https://doi.org/10.1098/rsta.2014.0374

Flemming, N. C. (1978). Holocene eustatic changes and coastal tectonics in the northeast mediterranean: Implications for models of crustal consumption. *Philosophical Transactions of the Royal Society of London - Series A: Mathematical and Physical Sciences*, *289*, 405–458. https://doi.org/10.1098/RSTA.1978.0065

Folch, A., Abril, C., Afanasiev, M., Amati, G., Bader, M., Badia, R. M., et al. (2023). The EU center of excellence for exascale in solid Earth (ChEESE): Implementation, results, and roadmap for the second phase. *Future Generation Computer Systems*, *146*, 47–61. https://doi.org/10.1016/j.future.2023.04.006

Fukao, Y. (1979). Tsunami earthquakes and subduction processes near deep-sea trenches. *Journal of Geophysical Research*, *84*(B5), 2303–2314. https://doi.org/10.1029/JB084iB05p02303

Gabriel, A.-A., Ampuero, J.-P., Dalguer, L. A., & Mai, P. M. (2013). Source properties of dynamic rupture pulses with off-fault plasticity. *Journal of Geophysical Research: Solid Earth*, *118*(8), 4117–4126. https://doi.org/10.1002/jgrb.50213

Gabriel, A.-A., Garagash, D. I., Palgunadi, K. H., & Mai, P. M. (2024). Fault size–dependent fracture energy explains multiscale seismicity and cascading earthquakes. *Science*, *385*(6707), eadj9587. https://doi.org/10.1126/science.adj9587

Gallovič, F., & Valentova, L. (2020). Earthquake stress drops from dynamic rupture simulations constrained by observed ground motions. *Geophysical Research Letters*, *47*(4), e2019GL085880. https://doi.org/10.1029/2019GL085880

Gallovič, F., & Valentová, L. (2023). Broadband strong ground motion modeling using planar dynamic rupture with fractal parameters. *Journal of Geophysical Research: Solid Earth*, *128*(6), e2023JB026506. https://doi.org/10.1029/2023JB026506

Galvez, P., Ampuero, J.-P., Dalguer, L. A., Somala, S. N., & Nissen-Meyer, T. (2014). Dynamic earthquake rupture modelled with an unstructured 3-D spectral element method applied to the 2011 M9 Tohoku earthquake. *Geophysical Journal International*, *198*(2), 1222–1240. https://doi.org/10.1093/gji/ggu203

Galvez, P., Dalguer, L. A., Ampuero, J. P., & Giardini, D. (2016). Rupture reactivation during the 2011 M_{W}9.0 tohoku earthquake: Dynamic rupture and ground-motion simulations. *Bulletin of the Seismological Society of America*, *106*(3), 819–831. https://doi.org/10.1785/0120150153

Ganas, A., Briole, P., Bozionelos, G., Barberopoulou, A., Elias, P., Tsironi, V., et al. (2020). The 25 October 2018 {\text{M}}_{W} = 6.7 Zakynthos earthquake (Ionian Sea, Greece): A low-angle fault model based on GNSS data, relocated seismicity, small tsunami and implications for the seismic hazard in the west Hellenic Arc. *Journal of Geodynamics*, *137*, 101731. https://doi.org/10.1016/j.jog.2020.101731

Ganas, A., & Parsons, T. (2009). Three-dimensional model of Hellenic Arc deformation and origin of the Cretan uplift. *Journal of Geophysical Research*, *114*(B6), 6404. https://doi.org/10.1029/2008JB005599

GEBCO Compilation Group. (2019). GEBCO 2019 grid. https://doi.org/10.5285/836f016a-33be-6ddc-e053-6c86abc0788e

Gibbons, S. J., Lorito, S., Macías, J., Løvholt, F., Selva, J., Volpe, M., et al. (2020). Probabilistic tsunami hazard analysis: High performance computing for massive scale inundation simulations. *Frontiers in Earth Science*, *8*, 591549. https://doi.org/10.3389/feart.2020.591549

Gómez Zapata, J. C., Pittore, M., Cotton, F., Lilienkamp, H., Shinde, S., Aguirre, P., & Santa María, H. (2022). Epistemic uncertainty of probabilistic building exposure compositions in scenario-based earthquake loss models. *Bulletin of Earthquake Engineering*, *20*(5), 2401–2438. https://doi.org/10.1007/s10518-021-01312-9

Granot, R. (2016). Palaeozoic oceanic crust preserved beneath the eastern mediterranean. *Nature Geoscience*, *9*, 701–705. https://doi.org/10.1038/ngeo2784

Graves, R., Jordan, T. H., Callaghan, S., Deelman, E., Field, E., Juve, G., et al. (2011). CyberShake: A physics-based seismic hazard model for southern California. *Pure and Applied Geophysics*, *168*(3–4), 367–381. https://doi.org/10.1007/s00024-010-0161-6

Grezio, A., Laura, S., Warner, M., Andrea, A., Paolo, G., & Jacopo, S. (2012). Probabilistic tsunami hazard assessment for Messina strait area (Sicily, Italy). *Natural Hazards*, *64*(1), 329–358. https://doi.org/10.1007/s11069-012-0246-x

Griffith, W. A., Nielsen, S., Di Toro, G., & Smith, S. A. F. (2010). Rough faults, distributed weakening, and off-fault deformation. *Journal of Geophysical Research*, *115*(B8). https://doi.org/10.1029/2009JB006925

Gu, Y., Zhang, Z., Wang, W., & Wang, Z. (2023). Dynamic rupture simulations based on interseismic locking models—Taking the Suoerkuli section of the Altyn Tagh fault as an example. *Geophysical Journal International*, *234*(3), 1737–1751. https://doi.org/10.1093/gji/ggad161

Guidoboni, E., & Comastri, A. (1997). The large earthquake of 8 August 1303 in Crete: Seismic scenario and tsunami in the mediterranean area. *Journal of Seismology*, *1*(1), 55–72. https://doi.org/10.1023/A:1009737632542

Guidoboni, E., & Comastri, A., & nazionale di geofisica e vulcanologia (Italy), I. (2005). In *Catalogue of earthquakes and tsunamis in the Mediterranean area from the 11th to the 15th century*. INGV Istituto Nazionale di Geofisica e Vulcanologia.

Hardebeck, J. L. (2015). Stress orientations in subduction zones and the strength of subduction megathrust faults. *Science*, *349*(6253), 1213–1216. https://doi.org/10.1126/science.aac5625

Harris, R. A., Barall, M., Aagaard, B., Ma, S., Roten, D., Olsen, K., et al. (2018). A suite of exercises for verifying dynamic earthquake rupture codes. *Seismological Research Letters*, *89*(3), 1146–1162. https://doi.org/10.1785/0220170222

Hok, S., Fukuyama, E., & Hashimoto, C. (2011). Dynamic rupture scenarios of anticipated Nankai-Tonankai earthquakes, southwest Japan. *Journal of Geophysical Research*, *116*(B12), B12319. https://doi.org/10.1029/2011JB008492

Ida, Y. (1972). Cohesive force across the tip of a longitudinal-shear crack and Griffith's specific surface energy. *Journal of Geophysical Research*, *77*(20), 3796–3805. https://doi.org/10.1029/JB077i020p03796

Ide, S., & Aochi, H. (2005). Earthquakes as multiscale dynamic ruptures with heterogeneous fracture surface energy. *Journal of Geophysical Research*, *110*(B11). https://doi.org/10.1029/2004JB003591

Jackson, J., & Mckenzie, D. (1988). The relationship between plate motions and seismic moment tensors, and the rates of active deformation in the Mediterranean and Middle East. *Geophysical Journal*, *93*(1), 45–73. https://doi.org/10.1111/j.1365-246X.1988.tb01387.x

Jeandet Ribes, L., Thomas, M. Y., & Bhat, H. S. (2023). On the importance of setting 3-D stress field in simulations of on- and off-fault deformation. *Geophysical Journal International*, *235*(3), 2962–2978. https://doi.org/10.1093/gji/ggad401

Jolivet, L., Faccenna, C., Huet, B., Labrousse, L., Le Pourhiet, L., Lacombe, O., et al. (2013). Aegean tectonics: Strain localisation, slab tearing and trench retreat. *Tectonophysics*, *597–598*, 1–33. (The Aegean: a natural laboratory for tectonics - Neotectonics). https://doi.org/10.1016/j.tecto.2012.06.011

Jongsma, D. (1977). Bathymetry and shallow structure of the Pliny and Strabo trenches, south of the Hellenic Arc. *GSA Bulletin*, *88*(6), 797–805. https://doi.org/10.1130/0016-7606(1977)88⟨797:BASSOT⟩2.0.CO;2

Kahle, H.-G., Cocard, M., Peter, Y., Geiger, A., Reilinger, R., Barka, A., & Veis, G. (2000). GPS-derived strain rate field within the boundary zones of the Eurasian, African, and Arabian Plates. *Journal of Geophysical Research*, *105*(B10), 353–376. https://doi.org/10.1029/2000JB900238

Kammer, D. S., McLaskey, G. C., Abercrombie, R. E., Ampuero, J.-P., Cattania, C., Cocco, M., et al. (2024). Energy dissipation in earthquakes. https://doi.org/10.48550/arXiv.2403.06916

Kaneko, Y., Avouac, J.-P., & Lapusta, N. (2010). Towards inferring earthquake patterns from geodetic observations of interseismic coupling. *Nature Geoscience*, *3*(5), 363–369. https://doi.org/10.1038/ngeo843

Kaneko, Y., & Fialko, Y. (2011). Shallow slip deficit due to large strike-slip earthquakes in dynamic rupture simulations with elasto-plastic off-fault response. *Geophysical Journal International*, *186*(3), 1389–1403. https://doi.org/10.1111/j.1365-246X.2011.05117.x

Käser, M., & Dumbser, M. (2006). An arbitrary high-order discontinuous galerkin method for elastic waves on unstructured meshes — I. The two-dimensional isotropic case with external source terms. *Geophysical Journal International*, *166*(2), 855–877. https://doi.org/10.1111/j.1365-246X.2006.03051.x

Käser, M., Hermann, V., & Puente, J. d. l. (2008). Quantitative accuracy analysis of the discontinuous Galerkin method for seismic wave propagation. *Geophysical Journal International*, *173*(3), 990–999. https://doi.org/10.1111/j.1365-246X.2008.03781.x

Ke, C.-Y., McLaskey, G. C., & Kammer, D. S. (2018). Rupture termination in laboratory-generated earthquakes. *Geophysical Research Letters*, *45*(23), 12784–12792. https://doi.org/10.1029/2018GL080492

Ke, C.-Y., McLaskey, G. C., & Kammer, D. S. (2022). Earthquake breakdown energy scaling despite constant fracture energy. *Nature Communications*, *13*(1), 1005. https://doi.org/10.1038/s41467-022-28647-4

Kelly, G. (2004). Ammianus and the great tsunami. *Journal of Roman Studies*, *94*, 141–167. https://doi.org/10.2307/4135013

Kim, Y.-S., & Sanderson, D. J. (2006). Structural similarity and variety at the tips in a wide range of strike–slip faults: A review. *Terra Nova*, *18*(5), 330–344. https://doi.org/10.1111/j.1365-3121.2006.00697.x

Kiratzi, A. (2013). The January 2012 earthquake sequence in the Cretan Basin, south of the Hellenic Volcanic Arc: Focal mechanisms, rupture directivity and slip models. *Tectonophysics*, *586*, 160–172. https://doi.org/10.1016/j.tecto.2012.11.019

Kiratzi, A., Papazachos, C., Özacar, A., Pinar, A., Kkallas, C., & Sopaci, E. (2022). Characteristics of the 2020 Samos earthquake (Aegean Sea) using seismic data. *Bulletin of Earthquake Engineering*, *20*(14), 7713–7735. https://doi.org/10.1007/s10518-021-01239-1

Kkallas, C., Papazachos, C. B., Scordilis, E. M., & Margaris, B. N. (2021). Active stress field of the Southern Aegean Sea subduction area from fault-plane solutions on the basis of different stress inversion approaches. *Journal of Geodynamics*, *143*, 101813. https://doi.org/10.1016/J.JOG.2020.101813

Krenz, L., Uphoff, C., Ulrich, T., Gabriel, A.-A., Abrahams, L. S., Dunham, E. M., & Bader, M. (2021). 3D acoustic-elastic coupling with gravity: The dynamics of the 2018 Palu, Sulawesi earthquake and tsunami. In *Proceedings of the international conference for high performance computing, networking, storage and analysis*. Association for Computing Machinery. https://doi.org/10.1145/3458817.3476173

Kutschera, F., Gabriel, A.-A., Wirp, S. A., Li, B., Ulrich, T., Abril, C., & Halldórsson, B. (2024). Linked and fully coupled 3d earthquake dynamic rupture and tsunami modeling for the húsavík–flatey fault zone in north Iceland. *Solid Earth*, *15*(2), 251–280. https://doi.org/10.5194/se-15-251-2024

Laigle, M., Sachpazi, M., & Hirn, A. (2004). Variation of seismic coupling with slab detachment and upper plate structure along the western Hellenic subduction zone. *Tectonophysics*, *391*(1–4), 85–95. https://doi.org/10.1016/J.TECTO.2004.07.009

Lay, T., Kanamori, H., Ammon, C. J., Koper, K. D., Hutko, A. R., Ye, L., et al. (2012). Depth-varying rupture properties of subduction zone megathrust faults. *Journal of Geophysical Research*, *117*(B4). https://doi.org/10.1029/2011JB009133

Le Pichon, X., & Angelier, J. (1981). The Aegean Sea. *Philosophical Transactions of the Royal Society of London - Series A: Mathematical and Physical Sciences*, *300*(1454), 357–372. https://doi.org/10.1098/rsta.1981.0069

Li, B., Gabriel, A.-A., Ulrich, T., Abril, C., & Halldorsson, B. (2023). Dynamic rupture models, fault interaction and ground motion simulations for the segmented húsavík-flatey fault zone, northern Iceland. *Journal of Geophysical Research: Solid Earth*, *128*(6), e2022JB025886. https://doi.org/10.1029/2022JB025886

Li, L., Switzer, A. D., Chan, C.-H., Wang, Y., Weiss, R., & Qiu, Q. (2016). How heterogeneous coseismic slip affects regional probabilistic tsunami hazard assessment: A case study in the South China sea. *Journal of Geophysical Research: Solid Earth*, *121*(8), 6250–6272. https://doi.org/10.1002/2016JB013111

Lindsey, E. O., Mallick, R., Hubbard, J. A., Bradley, K. E., Almeida, R. V., Moore, J. D., et al. (2021). Slip rate deficit and earthquake potential on shallow megathrusts. *Nature Geoscience*, *14*(5), 321–326. https://doi.org/10.1038/s41561-021-00736-x

Lorito, S., Selva, J., Basili, R., Romano, F., Tiberti, M., & Piatanesi, A. (2014). Probabilistic hazard for seismically induced tsunamis: Accuracy and feasibility of inundation maps. *Geophysical Journal International*, *200*(1), 574–588. https://doi.org/10.1093/gji/ggu408

Lorito, S., Selva, J., Basili, R., Romano, F., Tiberti, M. M., & Piatanesi, A. (2015). Probabilistic hazard for seismically induced tsunamis: Accuracy and feasibility of inundation maps. *Geophysical Journal International*, *200*(1), 574–588. https://doi.org/10.1093/GJI/GGU408

Lorito, S., Tiberti, M. M., Basili, R., Piatanesi, A., & Valensise, G. (2008). Earthquake-generated tsunamis in the Mediterranean Sea: Scenarios of potential threats to southern Italy. *Journal of Geophysical Research*, *113*(B1). https://doi.org/10.1029/2007JB004943

Lotto, G. C., Dunham, E. M., Jeppson, T. N., & Tobin, H. J. (2017). The effect of compliant prisms on subduction zone earthquakes and tsunamis. *Earth and Planetary Science Letters*, *458*, 213–222. https://doi.org/10.1016/J.EPSL.2016.10.050

Lotto, G. C., Jeppson, T. N., & Dunham, E. M. (2019). Fully coupled simulations of megathrust earthquakes and tsunamis in the Japan trench, Nankai trough, and cascadia subduction zone. *Pure and Applied Geophysics*, *176*(9), 4009–4041. https://doi.org/10.1007/s00024-018-1990-y

Lotto, G. C., Nava, G., & Dunham, E. M. (2017). Should tsunami simulations include a nonzero initial horizontal velocity? *Earth Planets and Space*, *69*(1), 1–14. https://doi.org/10.1186/s40623-017-0701-8

Lund, B., & Townend, J. (2007). Calculating horizontal stress orientations with full or partial knowledge of the tectonic stress tensor. *Geophysical Journal International*, *170*(3), 1328–1335. https://doi.org/10.1111/j.1365-246X.2007.03468.x

Ma, S. (2008a). A physical model for widespread near-surface and fault zone damage induced by earthquakes. *Geochemistry, Geophysics, Geosystems*, *9*(11). https://doi.org/10.1029/2008GC002231

Ma, S. (2008b). A physical model for widespread near-surface and fault zone damage induced by earthquakes. *Geochemistry, Geophysics, Geosystems*, *9*(11). https://doi.org/10.1029/2008GC002231

Ma, S. (2022). Dynamic off-fault failure and tsunamigenesis at strike-slip restraining bends: Fully-coupled models of dynamic rupture, ocean acoustic waves, and tsunami in a shallow bay. *Tectonophysics*, *838*, 229496. https://doi.org/10.1016/j.tecto.2022.229496

Ma, S., & Andrews, D. J. (2010). Inelastic off-fault response and three-dimensional dynamics of earthquake rupture on a strike-slip fault. *Journal of Geophysical Research*, *115*(B4). https://doi.org/10.1029/2009JB006382

Ma, S., & Beroza, G. C. (2008). Rupture dynamics on a bimaterial interface for dipping faults. *Bulletin of the Seismological Society of America*, *98*(4), 1642–1658. https://doi.org/10.1785/0120070201

Ma, S., & Hirakawa, E. T. (2013). Dynamic wedge failure reveals anomalous energy radiation of shallow subduction earthquakes. *Earth and Planetary Science Letters*, *375*, 113–122. https://doi.org/10.1016/j.epsl.2013.05.016

Ma, S., & Nie, S. (2019). Dynamic wedge failure and along-arc variations of tsunamigenesis in the Japan trench margin. *Geophysical Research Letters*, *46*(15), 8782–8790. https://doi.org/10.1029/2019GL083148

Madden, E. H., Bader, M., Behrens, J., Dinther, Y. V., Gabriel, A. A., Rannabauer, L., et al. (2020). Linked 3-D modelling of megathrust earthquake-tsunami events: From subduction to tsunami run up. *Geophysical Journal International*, *224*(1), 487–516. https://doi.org/10.1093/GJI/GGAA484

Madden, E. H., Ulrich, T., & Gabriel, A.-A. (2022). The state of pore fluid pressure and 3-D megathrust earthquake dynamics. *Journal of Geophysical Research: Solid Earth*, *127*(4), e2021JB023382. https://doi.org/10.1029/2021JB023382

Maechling, P., Deelman, E., Zhao, L., Graves, R., Mehta, G., Gupta, N., et al. (2007). Scec cybershake workflows—Automating probabilistic seismic hazard analysis calculations. In I. J. Taylor, E. Deelman, D. B. Gannon, & M. Shields (Eds.), *Workflows for e-science: Scientific workflows for grids* (pp. 143–163). : Springer. https://doi.org/10.1007/978-1-84628-757-2_10

Mai, P. M., Schorlemmer, D., Page, M., Ampuero, J.-P., Asano, K., Causse, M., et al. (2016). The earthquake-source inversion validation (SIV) project. *Seismological Research Letters*, *87*(3), 690–708. https://doi.org/10.1785/0220150231

Marafi, N. A., Eberhard, M. O., Berman, J. W., Wirth, E. A., & Frankel, A. D. (2019). Impacts of simulated M9 cascadia subduction zone motions on idealized systems. *Earthquake Spectra*, *35*(3), 1261–1287. https://doi.org/10.1193/052418EQS123M

Markoulaki, S. (1987). Hospital excavations at Kissamos. *Archaelogikon Deltion, Ser.*, *B2*, 558–563.

Marzocchi, W., Taroni, M., & Selva, J. (2015). Accounting for epistemic uncertainty in PSHA: Logic tree and ensemble modeling. *Bulletin of the Seismological Society of America*, *105*(4), 2151–2159. https://doi.org/10.1785/0120140131

McCaffrey, R. (1997). Influences of recurrence times and fault zone temperatures on the age-rate dependence of subduction zone seismicity. *Journal of Geophysical Research*, *102*(B10), 22839–22854. https://doi.org/10.1029/97JB01827

McCloskey, J., Antonioli, A., Piatanesi, A., Sieh, K., Steacy, S., Nalbant, S., et al. (2008). Tsunami threat in the Indian Ocean from a future megathrust earthquake west of Sumatra. *Earth and Planetary Science Letters*, *265*(1–2), 61–81. https://doi.org/10.1016/J.EPSL.2007.09.034

McClusky, S., Balassanian, S., Barka, A., Demir, C., Ergintav, S., Georgiev, I., et al. (2000). Global Positioning System constraints on plate kinematics and dynamics in the eastern Mediterranean and Caucasus. *Journal of Geophysical Research*, *105*(B3), 5695–5719. https://doi.org/10.1029/1999JB900351

Meng, L., Inbal, A., & Ampuero, J.-P. (2011). A window into the complexity of the dynamic rupture of the 2011 mw 9 tohoku-oki earthquake. *Geophysical Research Letters*, *38*(7). https://doi.org/10.1029/2011GL048118

Meng, X., Goulet, C., Milner, K., Graves, R., & Callaghan, S. (2023). Comparison of nonergodic ground-motion components from CyberShake and NGA-West2 datasets in California. *Bulletin of the Seismological Society of America*, *113*(3), 1152–1175. https://doi.org/10.1785/0120220049

Miyatake, T. (1992). Dynamic rupture processes of inland earthquakes in Japan weak and strong asperities. *Geophysical Research Letters*, *19*(10), 1041–1044. https://doi.org/10.1029/92GL01046

Molina-Ormazabal, D., Ampuero, J.-P., & Tassara, A. (2023). Diverse slip behaviour of velocity-weakening fault barriers. *Nature Geoscience*, *16*(12), 1200–1207. https://doi.org/10.1038/s41561-023-01312-1

Moschetti, M. P., Aagaard, B. T., Ahdi, S. K., Altekruse, J., Boyd, O. S., Frankel, A. D., et al. (2023). The 2023 US national seismic hazard model: Ground-motion characterization for the conterminous United States. *Earthquake Spectra*, *40*(2), 1190. https://doi.org/10.1177/87552930231223995

Müller, R. D., Sdrolias, M., Gaina, C., & Roest, W. R. (2008). Age, spreading rates, and spreading asymmetry of the world's ocean crust. *Geochemistry, Geophysics, Geosystems*, *9*(4). https://doi.org/10.1029/2007GC001743

Murotani, S., Miyake, H., & Koketsu, K. (2008). Scaling of characterized slip models for plate-boundary earthquakes. *Earth Planets and Space*, *60*(9), 987–991. https://doi.org/10.1186/BF03352855

Murphy, S., Scala, A., Herrero, A., Lorito, S., Festa, G., Trasatti, E., et al. (2016). Shallow slip amplification and enhanced tsunami hazard unravelled by dynamic simulations of mega-thrust earthquakes. *Scientific Reports*, *6*(1), 1–12. https://doi.org/10.1038/srep35007

Murphy, S., Toro, G. D., Romano, F., Scala, A., Lorito, S., Spagnuolo, E., et al. (2018). Tsunamigenic earthquake simulations using experimentally derived friction laws. *Earth and Planetary Science Letters*, *486*, 155–165. https://doi.org/10.1016/J.EPSL.2018.01.011

Necmioğlu, Ö., & Özel, N. M. (2014). An earthquake source sensitivity analysis for tsunami propagation in the Eastern Mediterranean. *Oceanography*, *27*(2), 76–85. https://doi.org/10.5670/oceanog.2014.42

Nielsen, S. B. (1998). Free surface effects on the propagation of dynamic rupture. *Geophysical Research Letters*, *25*(1), 125–128. https://doi.org/10.1029/97GL03445

Noda, A., Saito, T., Fukuyama, E., & Urata, Y. (2021). Energy-based scenarios for great thrust-type earthquakes in the Nankai trough subduction zone, southwest Japan, using an interseismic slip-deficit model. *Journal of Geophysical Research: Solid Earth*, *126*(5), e2020JB020417. https://doi.org/10.1029/2020JB020417

Nyst, M., & Thatcher, W. (2004). New constraints on the active tectonic deformation of the aegean. *Journal of Geophysical Research*, *109*(B11). https://doi.org/10.1029/2003JB002830

Oeser, J., Bunge, H.-P., & Mohr, M. (2006). Cluster design in the Earth sciences tethys. In M. Gerndt & D. Kranzlmüller (Eds.), *High performance computing and communications* (pp. 31–40). Springer.

Oral, E., Ampuero, J. P., Ruiz, J., & Asimaki, D. (2022). A method to generate initial fault stresses for physics-based ground-motion prediction consistent with regional seismicity. *Bulletin of the Seismological Society of America*, *112*(6), 2812–2827. https://doi.org/10.1785/0120220064

Ott, R. F., Wegmann, K. W., Gallen, S. F., Pazzaglia, F. J., Brandon, M. T., Ueda, K., & Fassoulas, C. (2021). Reassessing eastern mediterranean tectonics and earthquake hazard from the 365 CE earthquake. *AGU Advances*, *2*, e2020AV000315. https://doi.org/10.1029/2020AV000315

Palgunadi, K. H., Gabriel, A.-A., Ulrich, T., López-Comino, J. Á., & Mai, P. M. (2020). Dynamic Fault interaction during a fluid-injection-induced earthquake: The 2017 M_{W} 5.5 Pohang event. *Bulletin of the Seismological Society of America*, *110*(5), 2328–2349. https://doi.org/10.1785/0120200106

Panzera, F., Zechar, J. D., Vogfjörd, K. S., & Eberhard, D. A. (2016). A revised earthquake catalogue for South Iceland. *Pure and Applied Geophysics*, *173*(1), 97–116. https://doi.org/10.1007/s00024-015-1115-9

Papadimitriou, E. E., Karakostas, V., Mesimeri, M., & Vallianatos, F. (2016). The M_{W}6.7 2013 western Hellenic Arc main shock and its aftershock sequence: Implications for the slab properties. *International Journal of Earth Sciences*, *105*(7), 2149–2160. https://doi.org/10.1007/s00531-016-1294-3

Papadimitriou, E. E., & Karakostas, V. G. (2008). Rupture model of the great AD 365 Crete earthquake in the southwestern part of the Hellenic Arc. *Acta Geophysica*, *56*(2), 293–312. https://doi.org/10.2478/s11600-008-0001-6

Papadopoulos, G., Minoura, K., Imamura, F., Kuran, U., Yalçiner, A., Fokaefs, A., & Takahashi, T. (2012). Geological evidence of tsunamis and earthquakes at the eastern Hellenic Arc: Correlation with historical seismicity in the eastern Mediterranean Sea. *Research in Geophysics*, *2*, 12. https://doi.org/10.4081/rg.2012.e12

Papazachos, B. C., Karakostas, V. G., Papazachos, C. B., & Scordilis, E. M. (2000). The geometry of the Wadati–Benioff zone and lithospheric kinematics in the Hellenic arc. *Tectonophysics*, *319*(4), 275–300. https://doi.org/10.1016/S0040-1951(99)00299-1

Papazachos, B. C., & Nolet, G. (1997). P and S deep velocity structure of the Hellenic area obtained by robust nonlinear inversion of travel times. *Journal of Geophysical Research*, *102*(B4), 8349–8367. https://doi.org/10.1029/96JB03730

Papazachos, B. C., Papaioannou, C. A., Papazachos, C. B., & Savvaidis, A. S. (1999). Rupture zones in the Aegean region. *Tectonophysics*, *308*(1), 205–221. https://doi.org/10.1016/S0040-1951(99)00073-6

Papoulia, J., Tsambas, A., Anagnostou, C., Makris, J., Pomonis, A., Gulkan, P., et al. (2010). Seismic and tsunami risk assessment and mitigation scenarios in the western Hellenic Arc: The SEAHELLARC project. *14 ECEE*, *8*.

Pelties, C., de la Puente, J., Ampuero, J.-P., Brietzke, G. B., & Käser, M. (2012). Three-dimensional dynamic rupture simulation with a high-order discontinuous Galerkin method on unstructured tetrahedral meshes. *Journal of Geophysical Research*, *117*(B2). https://doi.org/10.1029/2011JB008857

Pelties, C., Gabriel, A.-A., & Ampuero, J.-P. (2014). Verification of an ADER-DG method for complex dynamic rupture problems. *Geoscientific Model Development*, *7*(3), 847–866. https://doi.org/10.5194/gmd-7-847-2014

Pichon, X. L., & Angelier, J. (1979). The Hellenic arc and trench system: A key to the neotectonic evolution of the eastern mediterranean area. *Tectonophysics*, *60*(1), 1–42. https://doi.org/10.1016/0040-1951(79)90131-8

Pirazzoli, P. A., Ausseil-Badie, J., Giresse, P., Hadjidaki, E., & Arnold, M. (1992). Historical environmental changes at phalasarna harbor, West Crete. *Geoarchaeology*, *7*(4), 371–392. https://doi.org/10.1002/GEA.3340070406

Pirazzoli, P. A., Laborel, J., & Stiros, S. C. (1996). Earthquake clustering in the Eastern Mediterranean during historical times. *Journal of Geophysical Research*, *101*(B3), 6083–6097. https://doi.org/10.1029/95jb00914

Pirazzoli, P. A., Thommeret, J., Thommeret, Y., Laborel, J., & Montag-Gioni, L. F. (1982). Crustal block movements from Holocene shorelines: Crete and Antikithera (Greece). *Tectonophysics*, *86*(1–3), 27–43. https://doi.org/10.1016/0040-1951(82)90060-9

Piromallo, C., & Morelli, A. (2003). P wave tomography of the mantle under the Alpine-Mediterranean area. *Journal of Geophysical Research*, *108*(B2). https://doi.org/10.1029/2002JB001757

Ramos, M. D., & Huang, Y. (2019). How the transition region along the Cascadia megathrust influences coseismic behavior: Insights from 2-D dynamic rupture simulations. *Geophysical Research Letters*, *46*(4), 1973–1983. https://doi.org/10.1029/2018GL080812

Ramos, M. D., Huang, Y., Ulrich, T., Li, D., Gabriel, A.-A., & Thomas, A. M. (2021). Assessing margin-wide rupture behaviors along the cascadia megathrust with 3-d dynamic rupture simulations. *Journal of Geophysical Research: Solid Earth*, *126*(7), e2021JB022005. https://doi.org/10.1029/2021JB022005

Ramos, M. D., Thakur, P., Huang, Y., Harris, R. A., & Ryan, K. J. (2022). Working with dynamic earthquake rupture models: A practical guide. *Seismological Society of America*, *93*(4), 2096–2110. https://doi.org/10.1785/0220220022

Reilinger, R., McClusky, S., Vernant, P., Lawrence, S., Ergintav, S., Cakmak, R., et al. (2006). GPS constraints on continental deformation in the Africa-Arabia-Eurasia continental collision zone and implications for the dynamics of plate interactions. *Journal of Geophysical Research*, *111*(B5). https://doi.org/10.1029/2005JB004051

Ren, C., Yue, H., Cao, B., Zhu, Y., Wang, T., An, C., et al. (2022). Rupture process of the 2020 {\text{M}}_{W}=6.9 Samos, Greece earthquake on a segmented fault system constrained from seismic, geodetic, and tsunami observations. *Tectonophysics*, *839*, 229497. https://doi.org/10.1016/j.tecto.2022.229497

Rice, J. R. (1980). The mechanics of earthquake rupture. In A. Dziewonski & E. Boschi (Eds.), *Physics of the earth's interior, proc. int. sch. phys. enrico fermi* (Vol. 78, pp. 555–649).

Ripperger, J., Mai, P., & Ampuero, J.-P. (2008). Variability of near-field ground motion from dynamic earthquake rupture simulations. *Bulletin of the Seismological Society of America*, *98*(3), 1207–1228. https://doi.org/10.1785/0120070076

Rodriguez-Marek, A., Bommer, J. J., Youngs, R. R., Crespo, M. J., Stafford, P. J., & Bahrampouri, M. (2021). Capturing epistemic uncertainty in site response. *Earthquake Spectra*, *37*(2), 921–936. https://doi.org/10.1177/8755293020970975

Roten, D., Olsen, K., Day, S., & Cui, Y. (2018). Quantification of fault-zone plasticity effects with spontaneous rupture simulations. *Best practices in physics-based fault rupture models for seismic hazard assessment of nuclear installations*, 45–67. https://doi.org/10.1007/978-3-319-72709-7_5

Roten, D., Olsen, K. B., & Day, S. M. (2017). Off-fault deformations and shallow slip deficit from dynamic rupture simulations with fault zone plasticity. *Geophysical Research Letters*, *44*(15), 7733–7742. https://doi.org/10.1002/2017GL074323

Roten, D., Olsen, K. B., Day, S. M., Cui, Y., & Fäh, D. (2014). Expected seismic shaking in Los Angeles reduced by San Andreas fault zone plasticity. *Geophysical Research Letters*, *41*(8), 2769–2777. https://doi.org/10.1002/2014GL059411

Rubin, A. M., & Ampuero, J. P. (2007). Aftershock asymmetry on a bimaterial interface. *Journal of Geophysical Research*, *112*(B5), 5307. https://doi.org/10.1029/2006JB004337

Ryan, K. J., Geist, E. L., Barall, M., & Oglesby, D. D. (2015). Dynamic models of an earthquake and tsunami offshore Ventura, California. *Geophysical Research Letters*, *42*(16), 6599–6606. https://doi.org/10.1002/2015GL064507

Saito, T., Baba, T., Inazu, D., Takemura, S., & Fukuyama, E. (2019). Synthesizing sea surface height change including seismic waves and tsunami using a dynamic rupture scenario of anticipated Nankai trough earthquakes. *Tectonophysics*, *769*, 228166. https://doi.org/10.1016/J.TECTO.2019.228166

Sallarès, V., & Ranero, C. R. (2019). Upper-plate rigidity determines depth-varying rupture behaviour of megathrust earthquakes. *Nature*, *576*(7785), 96–101. https://doi.org/10.1038/s41586-019-1784-0

Saltogianni, V., Mouslopoulou, V., Oncken, O., Nicol, A., Gianniou, M., & Mertikas, S. (2020). Elastic fault interactions and earthquake rupture along the southern Hellenic subduction plate interface zone in Greece. *Geophysical Research Letters*, *47*(13), e2019GL086604. https://doi.org/10.1029/2019GL086604

Savran, W. H., & Olsen, K. B. (2020). Kinematic rupture generator based on 3-D spontaneous rupture simulations along geometrically rough faults. *Journal of Geophysical Research: Solid Earth*, *125*(10), e2020JB019464. https://doi.org/10.1029/2020JB019464

Scala, A., Festa, G., & Vilotte, J. P. (2017). Rupture dynamics along bimaterial interfaces: A parametric study of the shear-normal traction coupling. *Geophysical Journal International*, *209*, 48–67. https://doi.org/10.1093/gji/ggw489

Scala, A., Lorito, S., Romano, F., Murphy, S., Selva, J., Basili, R., et al. (2020). Effect of shallow slip amplification uncertainty on probabilistic tsunami hazard analysis in subduction zones: Use of long-term balanced stochastic slip models. *Pure and Applied Geophysics*, *177*(3), 1497–1520. https://doi.org/10.1007/s00024-019-02260-x

Scheffers, A., & Scheffers, S. (2007). Tsunami deposits on the coastline of west Crete (Greece). *Earth and Planetary Science Letters*, *259*(3–4), 613–624. https://doi.org/10.1016/J.EPSL.2007.05.041

Schmedes, J., Archuleta, R. J., & Lavallée, D. (2010). Correlation of earthquake source parameters inferred from dynamic rupture simulations. *Journal of Geophysical Research*, *115*(B3). https://doi.org/10.1029/2009JB006689

Selva, J., Lorito, S., Volpe, M., Romano, F., Tonini, R., Perfetti, P., et al. (2021). Probabilistic tsunami forecasting for early warning. *Nature Communications*, *12*(1), 5677. https://doi.org/10.1038/s41467-021-25815-w

Selva, J., Tonini, R., Molinari, I., Tiberti, M. M., Romano, F., Grezio, A., et al. (2016). Quantification of source uncertainties in seismic probabilistic tsunami hazard analysis (SPTHA). *Geophysical Journal International*, *205*(3), 1780–1803. https://doi.org/10.1093/GJI/GGW107

Shaw, B., Ambraseys, N. N., England, P. C., Floyd, M. A., Gorman, G. J., Higham, T. F., et al. (2008). Eastern Mediterranean tectonics and tsunami hazard inferred from the AD 365 earthquake. *Nature Geoscience*, *1*(4), 268–276. https://doi.org/10.1038/ngeo151

Shaw, B., & Jackson, J. (2010). Earthquake mechanisms and active tectonics of the Hellenic subduction zone. *Geophysical Journal International*, *181*, 966–984. https://doi.org/10.1111/J.1365-246X.2010.04551.X

Shibazaki, B., & Matsu'ura, M. (1992). Spontaneous processes for nucleation, dynamic propagation, and stop of earthquake rupture. *Geophysical Research Letters*, *19*(12), 1189–1192. https://doi.org/10.1029/92GL01072

Soloviev, S. L., Solovieva, O. N., Go, C. N., Kim, K. S., & Shchetnikov, N. A. (2000). *Tsunamis in the Mediterranean Sea 2000 B.C.-2000 A.D.* (Vol. 13). Springer Science and Business Media.

Song, S. G., & Somerville, P. (2010). Physics-based earthquake source characterization and modeling with geostatistics. *Bulletin of the Seismological Society of America*, *100*(2), 482–496. https://doi.org/10.1785/0120090134

Sørensen, M. B., Spada, M., Babeyko, A., Wiemer, S., & Grünthal, G. (2012). Probabilistic tsunami hazard in the Mediterranean Sea. *Journal of Geophysical Research*, *117*(B1). https://doi.org/10.1029/2010JB008169

Souty, V., & Gailler, A. (2021). Fast high-resolution s-ptha along the western mediterranean sea coastlines. application to the bay of cannes. *Frontiers in Earth Science*, *9*, 765610. https://doi.org/10.3389/feart.2021.765610

Speranza, F., Minelli, L., Pignatelli, A., & Chiappini, M. (2012). The ionian sea: The oldest in situ ocean fragment of the world? *Journal of Geophysical Research*, *117*(B12). https://doi.org/10.1029/2012JB009475

Spratt, T. A. B. (1865). *Travels and researches in Crete* (Vol. 2). J. van Voorst.

Stiros, S., & Drakos, A. (2006). A fault-model for the tsunami-associated, magnitude geq 8.5 Eastern Mediterranean, AD365 earthquake. *Zeitschrift für Geomorphologie*, *146*, 125–137.

Stiros, S. C. (2010). The 8.5+ magnitude, AD365 earthquake in Crete: Coastal uplift, topography changes, archaeological and historical signature. *Quaternary International*, *216*(1–2), 54–63. https://doi.org/10.1016/j.quaint.2009.05.005

Stiros, S. C. (2020). The AD 365 Ammianus tsunami in Alexandria, Egypt, and the Crete ca. 365 fault and tsunami. *Arabian Journal of Geosciences*, *13*(15), 1–12. https://doi.org/10.1007/S12517-020-05667-2

Strasser, F. O., Arango, M. C., & Bommer, J. J. (2010). Scaling of the source dimensions of interface and intraslab subduction-zone earthquakes with moment magnitude. *Article in Seismological Research Letters*, *81*(6), 941–950. https://doi.org/10.1785/gssrl.81.6.941

Tarbali, K., Bradley, B. A., & Baker, J. W. (2018). Consideration and propagation of ground motion selection epistemic uncertainties to seismic performance metrics. *Earthquake Spectra*, *34*(2), 587–610. https://doi.org/10.1193/061317EQS114M

Taufiqurrahman, T., Gabriel, A.-A., Li, D., Ulrich, T., Li, B., Carena, S., et al. (2023). Dynamics, interactions and delays of the 2019 Ridgecrest rupture sequence. *Nature*, *618*(7964), 308–315. https://doi.org/10.1038/s41586-023-05985-x

Taufiqurrahman, T., Gabriel, A.-A., Ulrich, T., Valentová, L., & Gallovič, F. (2022). Broadband dynamic rupture modeling with fractal fault roughness, frictional heterogeneity, viscoelasticity and topography: The 2016 mw 6.2 amatrice, Italy earthquake. *Geophysical Research Letters*, *49*(22), e2022GL098872. https://doi.org/10.1029/2022GL098872

Taymaz, T., Jackson, J., & Westaway, R. (1990). Earthquake mechanisms in the hellenic trench near Crete. *Geophysical Journal International*, *102*(3), 695–731. https://doi.org/10.1111/j.1365-246X.1990.tb04590.x

Tinti, E., Casarotti, E., Ulrich, T., Taufiqurrahman, T., Li, D., & Gabriel, A.-A. (2021). Constraining families of dynamic models using geological, geodetic and strong ground motion data: The mw 6.5, october 30th, 2016, norcia earthquake, Italy. *Earth and Planetary Science Letters*, *576*, 117237. https://doi.org/10.1016/j.epsl.2021.117237

Tinti, S., Armigliato, A., Pagnoni, G., & Zaniboni, F. (2005). Scenarios of giant tsunamis of tectonic origin in the Mediterranean. *ISET Journal of Earthquake Technology*, *464*, 171–188. Paper No.

Tonini, R., Armigliato, A., Pagnoni, G., Zaniboni, F., & Tinti, S. (2011). Tsunami hazard for the city of Catania, eastern Sicily, Italy, assessed by means of worst-case Credible tsunami scenario analysis (WCTSA). *Natural Hazards and Earth System Sciences*, *11*(5), 1217–1232. https://doi.org/10.5194/NHESS-11-1217-2011

Tregoning, P., Brunner, F. K., Bock, Y., Puntodewo, S. S. O., McCaffrey, R., Genrich, J. F., et al. (1994). First geodetic measurement of convergence across the Java Trench. *Geophysical Research Letters*, *21*(19), 2135–2138. https://doi.org/10.1029/94GL01856

Ulrich, T., Gabriel, A.-A., Ampuero, J.-P., & Xu, W. (2019a). Dynamic viability of the 2016 {\text{M}}_{W} 7.8 Kaik\bar{o}ura earthquake cascade on weak crustal faults. *Nature Communications*, *10*(1), 1–16. https://doi.org/10.1038/s41467-019-09125-w

Ulrich, T., Gabriel, A.-A., & Madden, E. H. (2022). Stress, rigidity and sediment strength control megathrust earthquake and tsunami dynamics. *Nature Geoscience*, *15*(1), 67–73. https://doi.org/10.1038/s41561-021-00863-5

Ulrich, T., Vater, S., Madden, E. H., Behrens, J., van Dinther, Y., van Zelst, I., et al. (2019b). Coupled, physics-based modeling reveals earthquake displacements are critical to the 2018 Palu, Sulawesi tsunami. *Pure and Applied Geophysics*, *176*(10), 4069–4109. https://doi.org/10.1007/S00024-019-02290-5

Uphoff, C., Krenz, L., Ulrich, T., Wolf, S., Knoll, A., David, S., et al. (2022). SeisSol/SeisSol: v1.0.0-rc. *Zenodo*. https://doi.org/10.5281/zenodo.4672483

Uphoff, C., Rettenberger, S., Bader, M., Madden, E. H., Ulrich, T., Wollherr, S., & Gabriel, A. A. (2017). *Extreme scale multi-physics simulations of the tsunamigenic 2004 sumatra megathrust earthquake*. Association for Computing Machinery, Inc. https://doi.org/10.1145/3126908.3126948

Vannucci, G., Pondrelli, S., Argnani, A., Morelli, A., Gasperini, P., & Boschi, E. (2004). An atlas of Mediterranean seismicity. *Annals of Geophysics*, *47*(Suppl), 247–302.

van Zelst, I., Rannabauer, L., Gabriel, A.-A., & van Dinther, Y. (2022). Earthquake rupture on multiple splay faults and its effect on tsunamis. *Journal of Geophysical Research: Solid Earth*, *127*(8), e2022JB024300. https://doi.org/10.1029/2022JB024300

van Zelst, I., Wollherr, S., Gabriel, A.-A., Madden, E. H., & van Dinther, Y. (2019). Modeling megathrust earthquakes across scales: One-way coupling from geodynamics and seismic cycles to dynamic rupture. *Journal of Geophysical Research: Solid Earth*, *124*(11), 11414–11446. https://doi.org/10.1029/2019JB017539

Vernant, P., Reilinger, R., & McClusky, S. (2014). Geodetic evidence for low coupling on the Hellenic subduction plate interface. *Earth and Planetary Science Letters*, *385*, 122–129. https://doi.org/10.1016/J.EPSL.2013.10.018

Volpe, M., Lorito, S., Selva, J., Tonini, R., Romano, F., & Brizuela, B. (2019). From regional to local SPTHA: Efficient computation of probabilistic tsunami inundation maps addressing near-field sources. *Natural Hazards and Earth System Sciences*, *19*(3), 455–469. https://doi.org/10.5194/nhess-19-455-2019

Wei, X., Liu, Y., Xu, J., Liu, W., & Chen, X. (2024). A detailed understanding of slow self-arresting rupture. *Journal of Geophysical Research: Solid Earth*, *129*(8), e2024JB028881. https://doi.org/10.1029/2024JB028881

Wendt, J., Oglesby, D. D., & Geist, E. L. (2009). Tsunamis and splay fault dynamics. *Geophysical Research Letters*, *36*(15). https://doi.org/10.1029/2009GL038295

Weng, H., & Ampuero, J.-P. (2019). The dynamics of elongated earthquake ruptures. *Journal of Geophysical Research: Solid Earth*, *124*(8), 8584–8610. https://doi.org/10.1029/2019JB017684

Wesnousky, S. G. (2006). Predicting the endpoints of earthquake ruptures. *Nature*, *444*(7117), 358–360. https://doi.org/10.1038/nature05275

Wilson, A., & Ma, S. (2021). Wedge plasticity and fully coupled simulations of dynamic rupture and tsunami in the Cascadia subduction zone. *Journal of Geophysical Research: Solid Earth*, *126*(7), e2020JB021627. https://doi.org/10.1029/2020JB021627

Wirp, S. A., Gabriel, A. A., Ulrich, T., & Lorito, S. (2024). SeisSol model setup input files and supplement videos for the 3D dynamic rupture models of Wirp et al. 2024. *Zenodo*, https://doi.org/10.5281/zenodo.13285462

Wirp, S. A., Gabriel, A. A., Schmeller, M., Madden, E. H., van Zelst, I., Krenz, L., et al. (2021). 3D linked subduction, dynamic rupture, tsunami, and inundation modeling: Dynamic effects of supershear and tsunami earthquakes, hypocenter location, and shallow Fault Slip. *Frontiers in Earth Science*, *9*, 177. https://doi.org/10.3389/FEART.2021.626844

Wolf, S., Gabriel, A. A., & Bader, M. (2020). Optimization and local time stepping of an ADER-DG scheme for fully anisotropic wave propagation in complex geometries. In V. V. Krzhizhanovskaya (Ed.), *Computational science – iccs 2020* (pp. 32–45). Springer International Publishing.

Wollherr, S., Gabriel, A.-A., & Uphoff, C. (2018). Off-fault plasticity in three-dimensional dynamic rupture simulations using a modal discontinuous galerkin method on unstructured meshes: Implementation, verification and application. *Geophysical Journal International*, *214*(3), 1556–1584. https://doi.org/10.1093/gji/ggy213

Wong, J. W. C., Fan, W., & Gabriel, A.-A. (2023). A quantitative comparison and validation of finite-fault models: The 2011 Tohoku-Oki earthquake. *Authorea Preprints*. https://doi.org/10.22541/essoar.169203075.50034612/v1

Woo, G. (2018). Counterfactual disaster risk analysis. *Variance. J, Advancing the Science of Risk*, *10*, 279–291.

Xu, S., Ben-Zion, Y., Ampuero, J.-P., & Lyakhovsky, V. (2015). Dynamic ruptures on a frictional interface with off-fault brittle damage: Feedback mechanisms and effects on slip and near-fault motion. *Pure and Applied Geophysics*, *172*(5), 1243–1267. https://doi.org/10.1007/s00024-014-0923-7

Yang, H., Yao, S., He, B., Newman, A. V., & Weng, H. (2019). Deriving rupture scenarios from interseismic locking distributions along the subduction megathrust. *Journal of Geophysical Research: Solid Earth*, *124*(10), 10376–10392. https://doi.org/10.1029/2019JB017541

Yolsal, S., Taymaz, T., & Yalçiner, A. C. (2007). Understanding tsunamis, potential source regions and tsunami-prone mechanisms in the Eastern Mediterranean. *Geological Society - Special Publications*, *291*(1), 201–230. https://doi.org/10.1144/SP291.10

Yolsal-Çevikbilen, S., & Taymaz, T. (2012). Earthquake source parameters along the Hellenic subduction zone and numerical simulations of historical tsunamis in the Eastern Mediterranean. *Tectonophysics*, *536–537*, 61–100. https://doi.org/10.1016/j.tecto.2012.02.019

Zielke, O., Galis, M., & Mai, P. M. (2017). Fault roughness and strength heterogeneity control earthquake size and stress drop. *Geophysical Research Letters*, *44*(2), 777–783. https://doi.org/10.1002/2016GL071700